# A solid-state entangled photon pair source with high brightness and indistinguishability

Jin Liu,[1,*] Rongbin Su,[1,*] Yuming Wei,[1] Beimeng Yao,[1] Saimon Filipe Covre da Silva,[2] Ying Yu,[3] Jake Iles-Smith,[4] Kartik Srinivasan,[5] Armando Rastelli,[2,†] Juntao Li,[1,†] and Xuehua Wang[1,†]

[1]*State Key Laboratory of Optoelectronic Materials and Technologies, School of Physics, Sun Yat-sen University, Guangzhou 510275, China*

[2]*Institute of Semiconductor and Solid State Physics, Johannes Kepler University, Altenbergerstrae 69, Linz 4040, Austria*

[3]*State Key Laboratory of Optoelectronic Materials and Technologies, School of Electronics and Information Technology, Sun Yat-sen University, Guangzhou 510275, China*

[4]*School of Physics and Astronomy, The University of Sheffield, Sheffield, S10 2TN, United Kingdom*

[5]*Center for Nanoscale Science and Technology, National Institute of Standards and Technology, Gaithersburg, MD 20899, USA*

(Dated: December 16, 2018)

**The generation of high-quality entangled photon pairs has been being a long-sought goal in modern quantum communication and computation. To date, the most widely-used entangled photon pairs are generated from spontaneous parametric downconversion, a process that is intrinsically probabilistic and thus relegated to a regime of low pair-generation rates. In contrast, semiconductor quantum dots can generate triggered entangled photon pairs via a cascaded radiative decay process, and do not suffer from any fundamental trade-off between source brightness and multi-pair generation. However, a source featuring simultaneously high photon-extraction efficiency, high-degree of entanglement fidelity and photon indistinguishability has not yet been reported. Here, we present an entangled photon pair source with high brightness and indistinguishability by deterministically embedding GaAs quantum dots in broadband photonic nanostructures that enable Purcell-enhanced emission. Our source produces entangled photon pairs with a record pair collection probability of up to 0.65(4) (single-photon extraction efficiency of 0.85(3)), entanglement fidelity of 0.88(2), and indistinguishabilities of 0.901(3) and 0.903(3), which immediately creates opportunities for advancing quantum photonic technologies.**

Quantum entanglement is one of the most intriguing properties in quantum physics[1], in which the quantum state of a many-particle system cannot be written as a product of the single-particle wave functions, no matter how far they are separated from each other. Entangled photon pairs, which are immune from decoherence and are easy to manipulate and detect, have played an essential role in the epic triumph of quantum physics over local causality through optical tests of Bell's inequalities[2,3]. In the modern quantum technology era, entangled photon pairs serve as a key element in many quantum photonic information processing protocols[4,5], e.g., the quantum repeater[6] and device-independent quantum key distribution[7]. To date, spontaneous parametric down conversion (SPDC)[8–10] is the most widely used "working horse" for generating entangled-photon pairs with high degree of entanglement fidelity and photon indistingshability[11]. However, the Poissonian statistics of such sources intrinsically limits their brightness to an operation rate that is typically $< 0.1$[11] (the average photon pair generation probability per pulse), thus imposing a great challenge in advancing efficiency-demanding photonic quantum technologies.

Alternatively, epitaxial semiconductor quantum dots (QDs) have been successfully demonstrated as a potentially scalable technology for triggered sources of entangled photon pairs via the biexciton (XX) - exciton (X) cascaded radiative processes[12–17]. Their small footprint and compatibility with semiconductor technology make them particular appealing for on-chip integration[18]. However, a multitude of challenges have to be overcome to be able to realize optimal semiconductor sources of entangled photon pairs. First, the fine structure splitting (FSS) of the neutral exciton state, a result of the electron-hole exchange interaction in asymmetric QDs, reveals the radiative decay path information and consequently significantly reduces the time-averaged entanglement fidelity. This issue has been very recently alleviated by developing QDs with highly symmetric shapes, either by InGaAs growth in inverted pyramids[17] or by optimized droplet-etching[19]. Furthermore, it has been argued that the comparatively short radiative lifetime of X, the small nuclear spin number of Ga (3/2 compare to 9/2 of In), and the use of two-photon excitation effectively suppress the spin-flip and carrier recapture processes, thus facilitating the achievement of a high-degree of entanglement fidelity and indistinguishability[20,21].

Second, low photon extraction efficiency, a result of the high refractive index of the semiconductor material surrounding the QDs, has long been recognized as a hurdle for quantum light sources based on QDs. Typically, only $<1\%$ of the photons emitted by QDs in bulk material can be collected by a free-space lens or objective. Photonic nanostructures, e.g, cavities[22–24], waveguides[25–28], microlenses[29] and circular Bragg gratings[30,31], exhibit excellent performance in funneling the single-photons emitted by QDs into free-space or optical fibers, but directly implementing these nanostructures for entangled-photon pair generation is not straightforward. The state-of-the-art QD entangled photon pair sources are based on micro-pillar "molecules"[32], photonic nanowires[33] and optical antennas[34], in which each single-photon in the pair efficiently couples into a dedicatedly designed photonic channels, resulting in bright-entangled photon pairs with a high degree of entanglement fidelity. Nevertheless, the overall performance of these entangled pair sources must be significantly improved for most applications, in terms of simultaneously achieving high brightness, entanglement fidelity, and photon indistinguishability.

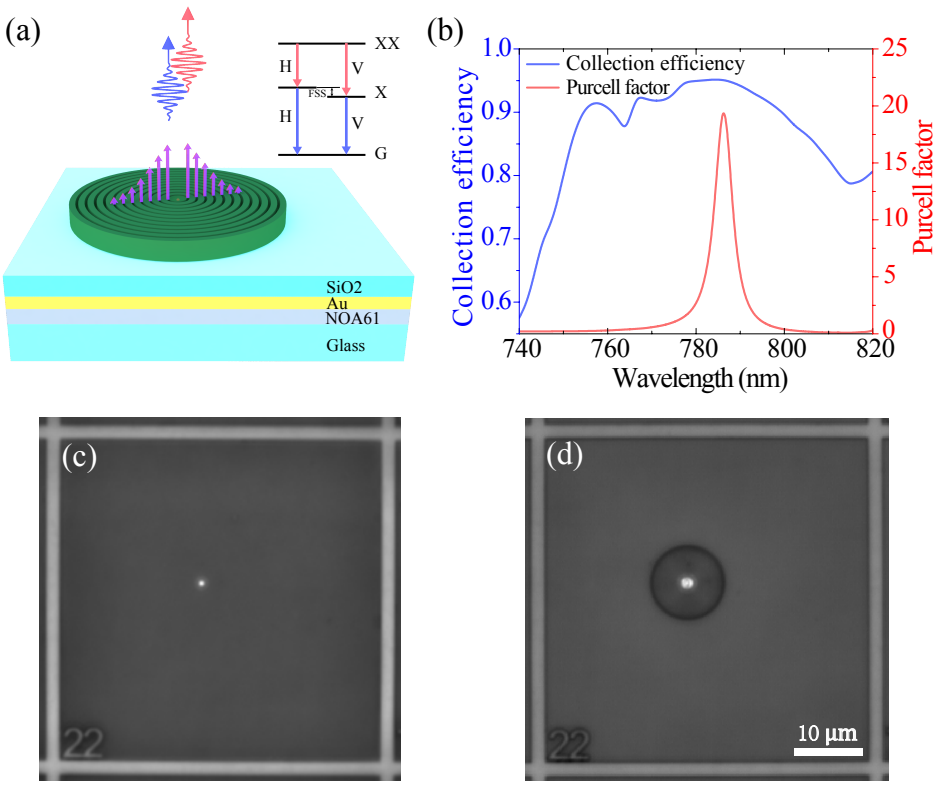


FIG. 1: Circular Bragg resonator on highly-efficient broadband reflector (CBR-HBR) for entangled-photon pair generation. Realization and calculated performance of the CBR-HBR are presented. (a) An illustration of a CBR-HBR with a single QD emitting entangled-photon pairs. The inset shows the XX-X cascaded radiative process for generating polarization-entangled photon pairs, in which the value of the fine structure splitting (FSS) plays an important role in determining the achievable entanglement fidelity without time-filtering. (b) Simulated Purcell factor (red) and collection efficiency (blue) of the CBR-HBR as a function of wavelength. The collection efficiency is based on a 40° azimuth angle, corresponding to a numerical aperture (NA) = 0.65. (c) and (d) are fluorescence images of the same QD before and after the fabrication of the CBR-HBR. (c) and (d) share the same scale bar.

Here we take a further step towards entangled photon pair sources with high brightness and indistinguishability by combining GaAs QDs with new broadband photonic nanostructures, i.e., circular Bragg resonators on highly-efficient broadband reflectors (CBR-HBR). Using a wide-field QD positioning technique[24,31,35], we deterministically fabricate CBR-HBRs in which single GaAs QDs (see S.I. I) are precisely located at the optimal position (the center of the cavity) for high-performance entangled photon pair generation. A single-photon collection efficiency of up to 0.85(3) for both X and XX is achieved, resulting in a record photon pair collection probability of 0.65(4) per excitation pulse. A high degree of single-photon purity of 99.8(1)%, entanglement fidelity of 0.88(2), and indistinguishabilities of 0.901(3) and 0.903(3) are also simultaneously obtained.

### Design and fabrication of devices

In order to realize bright entangled photon pairs with Purcell-enhanced emission rates, we have developed a new nanostructure, i.e., CBR-HBR, with a few significant advantages respective to our previous work[31]. Most notably, the implementation of the HBR strucuture effectively suppresses the downwards photon leakage and therefore significantly improves the collection efficiency over a broadband, see the details in the S.I. II. Our CBR-HBR consists of a circular AlGaAs disk surrounded by a set of concentric AlGaAs rings, sitting on a $SiO_2$ layer with a gold back reflector, as schematically shown in Fig. 1(a). The cavity resonance can be accurately engineered by varying the diameter of the central AlGaAs disk. Meanwhile, the in-plane emission is directed upwards by the concentric rings that meet the second-order Bragg conditions. By carefully designing the thickness of the $SiO_2$ insulator layer, all the photons leaking into the substrate can be effectively reflected from the broadband gold mirror and recaptured by the CBR (See more details in S.I. III). In such a situation, very high collection efficiencies can be obtained in a broadband manner. For QDs located in the center of the CBR, the simulated collection efficiency at the first lens and the Purcell factor as a function of the operation wavelength are plotted in Fig. 1(b). Collection efficiencies above

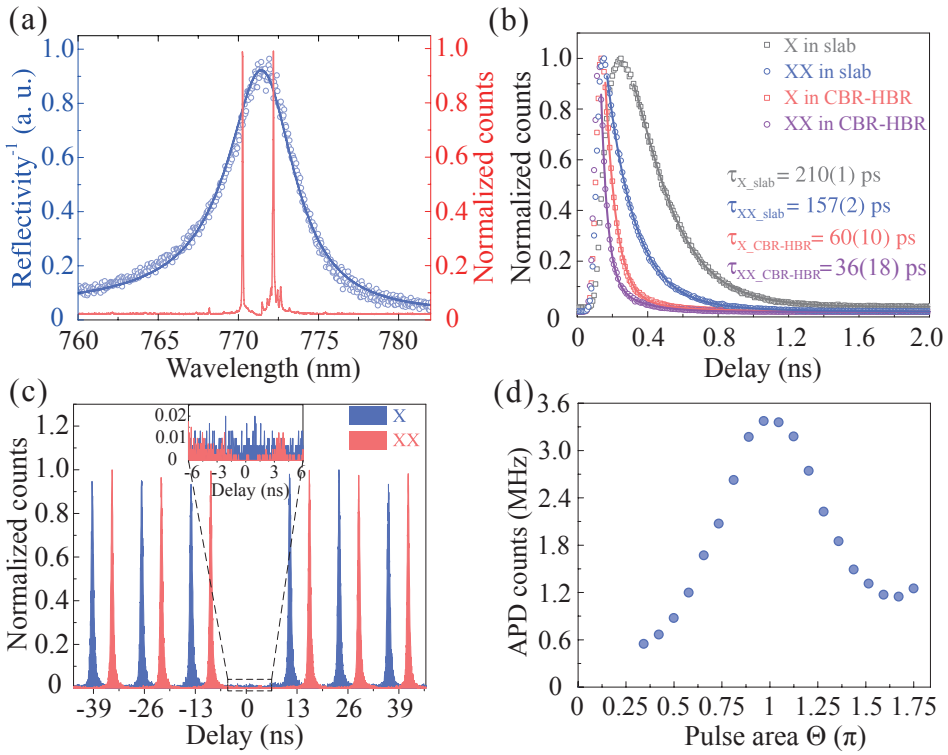


FIG. 2: **Basic characterization of the QD-CBR-HBR device.** (a) PL spectrum of a QD in the CBR-HBR under two-photon resonant excitation (right y axis, indicated in red) and the cavity mode measured from white light reflection (left y axis, indicated in blue). The excitation power is chosen to maximize the intensity of the XX emission ("π pulse" conditions), X and XX are equally populated and resonant with the cavity mode of the CBR-HBR. (b) PL lifetime of X and XX in bulk and in the CBR-HBR, showing pronounced Purcell enhancement for both X and XX. (c) Photon auto-correlation measured under "π pulse" two-photon resonant excitation, using a Hanbury-Brown and Twiss interferometer. The second-order correlation $g^{(2)}(0) = 0.001 \pm 0.001$ for X and $g^{(2)}(0) = 0.007 \pm 0.001$ for XX are calculated from the integrated area in the zero delay peak divided by the mean of the peaks away from zero-delay, and the uncertainty is a one standard deviation value. (d) Detected count rates of the X photons as a function of square root of the excitation power. The blue curve is a guide to the eyes.

90 % can be theoretically achieved in a bandwidth of ≈33 nm, and Purcell factors above 2 can be obtained for a bandwidth of ≈13 nm, which is 6.5 times the X-XX separation (≈2 nm).

We have developed a membrane transfer technique to realize the AlGaAs/$SiO_2$/Au material platform from which the CBR-HBRs are fabricated, with the details provided in the S.I. IV. We note that the presented photonic design is fully compatible with state-of-the-art piezoelectric-based tuning methods[36–38], which enable the elimination of the FSS and the tuning of photon energy because of the flexible choice of substrate (here quartz) and flat morphology, which allows efficient strain transfer. By taking advantage of our recently developed QD positioning technique, we are able to identify individual QDs and extract their spatial positions with respect to alignment marks with an uncertainty of ≈10 nm[31,35], see Fig. 1(c). The CBR-HBR is then deterministically fabricated around the target QD. Figure 1(d) shows the fluorescence image of our device after the CBR-HBR fabrication, in which the targeted single QD in Fig. 1(c) is accurately located in the center of the fabricated CBR-HBR.

## I. SINGLE-PHOTON EMISSION AND BRIGHTNESS ASSESSMENT

Figure 2(a) presents the photoluminescence (PL) and white light reflectivity (1/R is shown, with R the reflectivity spectrum) of our device at 3.2 K, see the optical setup in S.I. V. Under a pulsed two-photon resonant excitation (TPE) scheme[16,20,21,38,39], the intensities of the XX and X recombination are comparable, since TPE populates the XX state, which feeds the X state. The cavity mode, with a quality factor of ≈150, is clearly identified via the reflectivity measurement (see more details in S.I. VI) and it is resonant with both X and XX. The Purcell enhancement of the radiative decay of each state enabled by the cavity mode is directly quantified from time-resolved measurements in Fig. 2(b), showing comparisons of the lifetimes of X and XX in the CBR-HBR and in bulk (a different reference QD). We note the lifetimes of our reference QD in bulk are very consistent with the values reported in the similar systems[20,21]. The lifetime of X is shortened from 210 ps to 60 ps by implementing the CBR-HBR, corresponding to a Purcell factor ($F_p$) of 3.5. A slightly higher Purcell factor of 4.4 for XX is obtained, due to a better

spectral match to the cavity mode, which enables faster triggering rates of entangled photon pair emission compared to those of the QDs in bulk.

Second-order auto-correlation measurements are performed for both X and XX, see Fig. 2(c). The nearly complete absence of coincidence events at zero time delay indicates the ultra-high purity of the emitted single-photons. $g_X^{(2)}(0) = 0.001(1)$ and $g_X^{(2)}(0) = 0.007(1)$ are obtained without background correction. The slightly higher $g_{XX}^{(2)}(0)$ value of XX is mostly due to the very weak emission from neighboring QD states.

Different from the single-photon Rabi oscillation in which the population of the excited state is dependent on the pulse area, the pulse area in the two-photon Rabi oscillation is replaced by an adiabatic dynamic phase that turns out to be a non-trivial function of the quantum dot binding energy, pulse area, pulse duration and pulse shape[40]. Fig. 2(d) shows the detected photon flux from X as a function of the square root of the time-averaged excitation power. The Rabi oscillations of X and XX (not shown) are observed due to the coherent control of the two-level system consisting of the biexciton and crystal-ground-state in the QD. For this device, the photon count rate reaches a maximum for an average laser power of 36 nW, which we denote as "$\pi$ pulse" condition, similar to recent reports[16,21]. We note that the laser power needed to reach "$\pi$ pulse" for the QDs in a CBR-HBR is at least 200 times lower than that for QDs in the bulk and also in simple planar cavities. Such a reduction of "$\pi$ pulse" power is attributed to the cavity enhanced excitation[41] and represents an advantage for filtering the excitation laser in the entanglement and indistinguishability measurements we shall present.

For a "$\pi$ pulse", we observe a photon count rate up to 3.4(1) MHz under a 79 MHz repetition rate laser excitation. By taking the setup efficiency $\xi$ (7 %, see S.I. VII ), avalanche photodiode (APD) correction factor (1.25), and XX preparation fidelity $\eta_{XX}$ ($\approx$0.9) into account, a collection efficiency (with a 0.65 NA objective) $\eta$=85(3) % is extracted for both X and XX. Consequently, the collected photon pair probability per pulse $p = \eta_{XX} \times \eta^2 \times [1 - g_X^{(2)}(0)]^{1/2} \times [1 - g_{XX}^{(2)}(0)]^{1/2} = 0.65(4)$ is obtained. *This high photon pair rate per pulse $p \approx 0.65$ outperforms any of the existing entangled photon sources reported in the literature.*

### Entanglement characterization

The states of the photon pairs emitted by QDs can be written as $|\psi\rangle = 1/\sqrt{2}(|H_X H_{XX}\rangle + e^{is\tau/\hbar}|V_{XX}V_X\rangle)$[16,20,21,42], in which $\tau$ is the, statistically varying, decay time of the XX state relative to the decay time of the X state and s is the value of the FSS. In absence of other dephasing mechanisms, the deviation of the two-photon states from the Bell state $|\psi^+\rangle$ originates from the phase factor $s\tau/\hbar$, which has to be minimized in order to obtain high level of entanglement without resorting to inefficient time-filtering[43] or spectra-filtering[14]. Since the X lifetime $\tau_X$ is as short as 60 ps in our device thanks to the Purcell effect (corresponding to a lifetime-limited linewidth of $\sim$11 $\mu$eV), we expect that the generation of photon pairs with high time-averaged fidelity is still possible for QDs with a finite FSS. Using polarization-dependent measurements, shown in Fig. 3(a), a FSS of 4.8(2) $\mu$eV for the QD in the CBR-HBR is extracted by subtracting the X transition from the XX transition energy. The theoretical values of fidelity[44] as a function of FSS for different QDs with varied lifetimes are plotted in Fig. 3(b) (see the details in S.I. VIII). For GaAs QDs with a Purcell factor of 3.5, the entanglement fidelity decays slowly with the increase of the FSS. The predicted fidelity for the GaAs QDs with a FSS of 4.8 $\mu$eV is as high as 0.92 and it can still be above 0.75 for a FSS of 10 $\mu$eV. On the contrary, the entanglement fidelity for GaAs QDs in bulk (lifetime of 210 ps) decreases much more quickly with the increase of the FSS and shows a slightly lower value than the Purcell-enhanced source at FSS=0. With the same FSS of 4.8 $u$eV, the entanglement fidelity is only 0.64 for GaAs QDs in bulk. In order to compare the performance against a different material system, we also plot the entanglement fidelities of Purcell-enhanced InAs QDs ($F_p = 3.5$) and InAs QDs in bulk (typical lifetime of 1000 ps). For the InAs QDs in bulk, the highest fidelity is $< 0.75$ and the entanglement disappears once the FSS is larger than 1.6 $\mu$eV. Even with the same Purcell factor of 3.5, the entanglement fidelity of InAs QDs is still not reaching to the level of GaAs QDs in bulk. These results are based on the spin-scattering times provided in Ref. 20,21 and need further experimental confirmations.

To evaluate the degree of entanglement of our bright photon-pair source, we perform cross-correlation measurements under $\pi$ pulse excitation for both X and XX photons in linear (HV), diagonal (DA), and circular (LR) basis sets. The cross-correlation histograms in the three basis sets are presented in Fig. 3(c-e). In linear and diagonal basis sets, we clearly observe the antibunching when the photon pairs are co-polarized and bunching for the cross-polarized photon pairs. The correlation in the circular basis is just opposite: co-polarized photon pairs show bunching while cross-polarized ones exhibit antibunching behavior. This set of correlations serves as a strong indication of polarization entanglement in the photon pairs. The degree of correlation in a particular polarization basis is defined by[44]:

$$C_\mu = \frac{g_{XX,X}^{(2)}(0) - g_{XX,\bar{X}}^{(2)}(0)}{g_{XX,X}^{(2)}(0) + g_{XX,\bar{X}}^{(2)}(0)}$$

where $g_{XX,X}^{(2)}(0)$ and $g_{XX,\bar{X}}^{(2)}(0)$ are the second order correlation for the co-polarized and cross-polarized photon pairs in that basis at zero delay time. The extracted degree of correlation in the different basis sets from measured coincidence histograms are:

$$C_{linear} = 0.92(2)$$
$$C_{diagonal} = 0.81(2)$$
$$C_{circular} = -0.80(2)$$

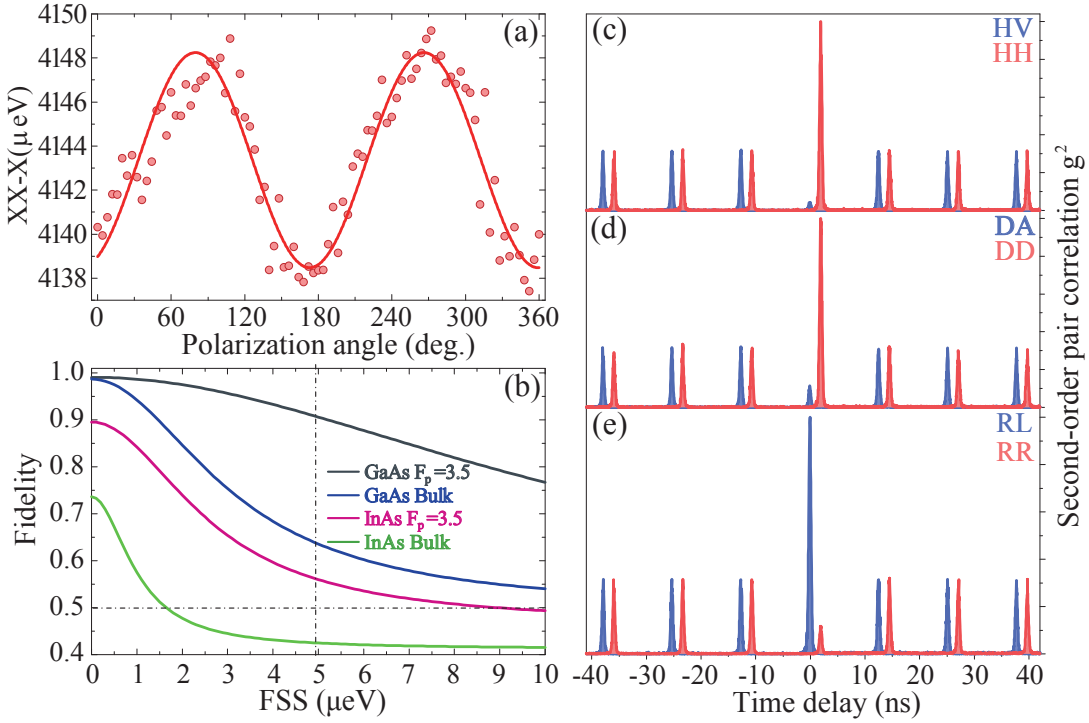


FIG. 3: **Entanglement characterization.** Fidelity of the polarization entanglement is investigated. (a) Polarization-dependent measurement to determine the FSS of X. The relative energy difference between X and XX is plotted in order to obtain a higher measurement precision. An FSS value of 4.8(2) $\mu$eV is extracted from the amplitude of the sine-function fitting. (b) Theoretically predicted entanglement fidelity as a function of FSS for GaAs QDs in the CBR-HBR ($F_p = 3.5$, black line), in bulk (blue line), Purcell enhanced InAs QDs ($F_p = 3.5$, ruby line) and InAs QDs in bulk (green line). The vertical dashed line denotes a FSS of 4.8 $\mu$eV and the horizontal dashed line ($f = 0.5$) is the boundary above which quantum entanglement exists. (c), (d) and (e) are the X-XX polarization dependent cross-correlation histogram under "$\pi$ pulse" conditions for linear, diagonal, and circular basis respectively. Data for cross-polarization configurations are shifted deliberately for clarity.

With these numbers, the entanglement fidelity for the polarization between the emitted photon pairs can be calculated as:

$$f = \frac{1 + C_{linear} + C_{diagonal} - C_{circular}}{4} = 0.88(2)$$

The theoretically predicted entanglement fidelity of 0.92 can be reduced to 0.88 by using a much shorter spin scattering time (1 ns instead of 15 ns), which strongly indicates the existence of extra dephasing processes. Such extra dephasing processes have been also recently observed in a similar material system and is attributed to the interactions between the confined exciton and charge states[38]. In contrast to existing entangled sources with vanishing FSS, the pronounced Purcell effect in our work makes the high fidelity of entanglement possible for QDs with a comparatively large FSS. A near-unity entanglement fidelity can be expected in the future by implementing GaAs QDs with very small FSS in CBR-HBRs or by eliminating the residual FSS with a strain-tunable CBR-HBR[38](see strain-tunable CBR-HBR in the S.I. IX).

### Photon indistinguishability

Photon indistinguishablity is a prerequisite for the realization of long-haul quantum information processing, e.g., a quantum repeater via entanglement swapping[45]. We study the indistinguishablity of the emitted photons from our device via Hong-Ou-Mandel (HOM) interference measurements[46]. The QD is excited by two $\pi$-pulses separated by 1.9 ns with a repetition rate of 79 MHz (13 ns period). The emitted single photons are spectrally filtered within windows of $\sim$100 $\mu$eV, much larger than the zero-phonon-linewidths of the transitions, and projected to the horizontal polarization before being coupled to an unbalanced Mach-Zehnder interferometer (MZI) equipped with a 1.9 ns delay. A half-wave plate is placed in one arm of the MZI to prepare co-polarized or cross-polarized photons, making them distinguishable or indistinguishable in polarization. The emitted photons are interfered at the beam splitter in co- and cross-polarized configurations. The coincidence histogram of HOM interference for both X and XX are shown in Fig. 4. For both X and XX, the coincidence events at zero delay are greatly suppressed in the co-polarized configuration (Fig. 4(a,b)), which indicates the occurrence of two-photon interference at the beam splitter. In contrast, the area of the central peaks are almost the same as the side peaks in the cross-polarized configuration, showing no indistinguishability (Fig. 4(c,d)). Visibilities of two-photon interference of 0.901(3) and 0.903(3) for X and XX are extracted from the areas of the central peaks in the correlation

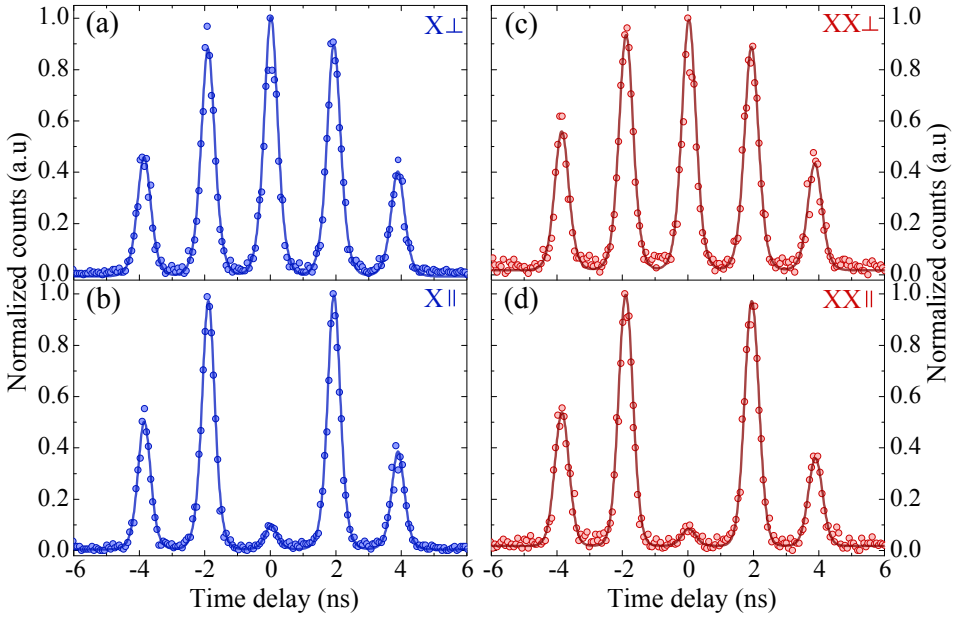


FIG. 4: **Photon indistinguishability.** HOM interference for X and XX photons are performed individually. Two-photon interference for cross-polarized (a), co-polarized (b) X photons and cross-polarized (c), co-polarized (d) XX photons. The data are fitted by exponential decays (measured emitter decay response) convolved with a Gaussian (measured photon detector time response). The area of the central peaks is extracted to calculate the raw visibilities, which are 0.901(3) and 0.903(3) for X and XX respectively.

TABLE I: Characterization of more devices from the same chip.

| **Device #** | **Single-photon efficiency/Pair rate** | **Cavity wavelength (nm)** | **X wavelength (nm)** | **X Purcell factor** | **FSS ($\mu$eV)/f** | **X HOM** | **XX HOM** |
|---|---|---|---|---|---|---|---|
| **1** | 0.86/0.65 | 772.43 | 770.05 | 3.5 | 4.8/0.88 | 0.9 | 0.9 |
| **2** | 0.80 | 769.36 | 770.86 | 2.6 | 11.6/N.A. | N.A. | N.A. |
| **3** | 0.76 | 767.39 | 777.51 | 3.1 | 18.0/N.A. | N.A. | N.A. |
| **4** | 0.70/0.44 | 767.18 | 778.91 | 3.1 | 3.4/0.85 | 0.81 | 0.84 |
| **5** | 0.67 | 766.17 | 767.08 | 1.7 | 5.8/N.A. | N.A. | N.A. |
| **6** | 0.66 | 763.86 | 765.08 | 2.1 | 11.0/N.A. | N.A. | N.A. |
| **7** | 0.63 | 766.76 | 766.18 | 2.7 | 9.1/N.A. | N.A. | N.A. |
| **8** | 0.61 | 767.20 | 770.20 | 3.4 | 5.1/N.A. | N.A. | N.A. |
| **9** | 0.56 | 765.53 | 769.51 | 2.2 | 15.8/N.A. | N.A. | N.A. |
| **10** | 0.55 | 764.24 | 766.62 | 2.0 | 6.6/N.A. | N.A. | N.A. |

histogram. We note that the high degree of photon indistinguishability in our pair source is a direct result of the Purcell effect, which has been recently shown as a key element to realizing highly indistinguishable single-photons from InAs QDs in micropillar cavities[22–24]. With a joint force of further improvement of the Purcell factor, charge-stabilization[23,47] and rapid adiabatic passage excitation[48], higher photon indistinguishability can be expected as well as the entanglement fidelity. However, in our devices, the collection effiency tends to decrease with higher Q-factors (therefore higher Purcell factors) of the cavity due to the reduction of the overlap between the far-field pattern and the objective. Ultimately, the simultaneous realization of high collection efficiency and high indistinguishability will be fundamentally limited by the phonon scattering process. An upper bound can be placed on the indistinguishability by considering the microscopic theory developed in Ref. 49. This theory uses the polaron master equation formalism to capture non-Markovian phonon processes that lead to the emergence of a phonon sideband in the QD emission spectrum, and consequently degrades the indistinguishability of the source. Using this formalism with standard GaAs parameters, we find that our source could have an indistinguishability as high as 0.98 in the absence of any other dephasing processes (e.g. charge noise), see the S.I. X for details of the calculation. However, moderate filtering of the phonon sidebands (at the expense of a few percent count reduction) may be used to further boost the indistinguishability.

While we focus on the performance of a single exemplary device, we have characterized several other devices on the same chip. In table 1 we have listed 10 such devices in the order of the brightness, among which 2 devices with the smallest FSSs are fully characterized (see S.I. XI) and the others are partially characterized. The device 4 has smallest FSS

TABLE II: Comparison of the performance of our device to the state-of-the-art entangled sources.

| | Pair efficiency[a] | Entanglement Fidelity | Indistinguishability |
|---|---|---|---|
| **InAs QD in micropillar molecule (Ref 32)** | 0.12 | 0.63 | Not shown |
| **InAsP QDs in nanowires (Ref 33)** | 0.0025 | 0.817 | Not shown |
| **InAs QDs in planar cavities (Ref 16)** | <0.0001 | 0.81 | 0.86 |
| **GaAs QDs in planar cavities (Ref 21)** | <0.0001 | 0.94 | 0.93 |
| **SPDC USTC (Ref 10)** | ∼0.1 | 0.93 | 0.91 |
| **SPDC Vienna (Ref 2)** | < 0.01 | >0.95 | >0.9 |
| **SPDC Geneva (Ref 9)** | < 0.1 | ∼0.9 | ∼0.9 |
| **This work** | 0.65(4) | 0.88(2) | ∼0.9 |

[a] The photon pair source efficiency is defined by the probability of collecting a photon pair per excitation pulse into the first collection optics, such as an objective or an optical fiber.

of 3.4 $\mu$eV and the device 1 has the second smallest FSS of 4.8 $\mu$eV with the highest Purcell factor of 3.5. Therefore we do not expect any higher entanglement fidelity in the other devices. The limiting factor of the entanglement fidelity in this batch of devices is the relative large FSSs of the GaAs droplet QDs grown in the thin membrane (140 nm) structure with a thick sacrificial layer (500 nm), as shown in Fig. S1(a). We believe such a limitation can be soon overcome by either optimizing the epitaxial growth process or developing the strain-tunable CBR-HBR that we proposed.

## Summary

Given the rapid development of the entangled photon sources both with SPDC and QD technologies, it is very insightful to directly compare the performance of our device to those of the existing sources reported in the literature. Table 2 lists the efficiency, entanglement fidelity, and indistinguishability of the state-of-the-art entangled photon sources together with our device (reference S.I. XII for methodology used in extracting the various parameters.). In general, the SPDC sources exhibit excellent performance in terms of entanglement fidelity and photon indistinguishability; however, their efficiencies are intrinsically limited to <0.1 due to the nature of the Poissonian statistics. Increasing the photon pair flux through higher excitation power inevitably adds extra noise and reduces the purity and indistinguishability. For the deterministic approach, the efficiency of QDs in bulk suffers greatly from the total internal reflection and only a few works show a high-degree of indistinguishability. InAsP QDs in nanowires and InAs QDs in micropillar molecules show much improved brightness and decent entanglement fidelity, but still the source efficiency and indistingshability have to be further improved. Our device, for the first time, simultaneously combines a high pair collection probability (0.65(4)), high degree of entanglement fidelity (0.88(2)) and photon indistinguishability (0.901(3) and 0.903(3)), and when taken together outperforms all the existing entangled photon pair sources.

To conclude, we have implemented a broadband photonic nanostrucuture, CBR-HBR, to harvest highly-entangled photon pairs emitted by GaAs QDs, obtained by droplet etching. By employing the QD positioning technique based on fluorescence imaging, the QDs are accurately placed in the center of the CBR-HBR, thus enabling the realization of entangled sources with record performances. Our devices may immediately find applications in both fundamental physics and applied quantum technologies, e.g., quantum random walk with entangled photon pairs[50], generation of hyper-entanglement[51] and quantum repeaters[6] associated with quantum memories. Moving forward, realizing high-performance photon pair sources operating in the telecom band[52,53] is particularly appealing for long-haul quantum communication. Instead of polarization entanglement, time-bin entanglements[39] can be directly generated from QDs, which makes our devices compatible with the fiber network. The operation wavelength for both droplet QDs and photonic nanostructures can be shifted to the telecom band by changing the filling material of the nanohole and scaling the size of the nanostructures. To scale this technology up to multiple QDs, piezo-tuning[36,37] or on-chip quantum frequency conversion technologies[54] can be directly implemented in our devices to tune the QD emission wavelength, overcome the spectral inhomogeneity between different QDs and eliminate the FSS. Such identical entangled pair sources can serve as individual nodes interconnected via single-photon interference in the future quantum network[55]. With the potential of scalability, our work serves as a landmark in the development of semiconductor quantum information processing chips and may boost new breakthroughs in quantum photonic technologies.

## References

* These authors contributed equally
† Correspondence to Armando.Rastelli@jku.at, lijt3@mail.sysu.edu.cn, wangxueh@mail.sysu.edu.cn

[1] Einstein, A., Podolsky, B., and Rosen, N., Can Quantum-

Mechanical Description of Physical Reality Be Considered Complete?, *Phys. Rev.* **47**, 777 (1935).

[2] Giustina, M., et al. Significant-Loophole-Free Test of Bell's Theorem with Entangled Photons. *Phys. Rev. Lett.* **115**, 250401 (2015).

[3] Shalm, L. K., et al. Strong Loophole-Free Test of Local Realism. *Phys. Rev. Lett.* **115**, 250402 (2015).

[4] Bouwmeester, D., Ekert, A. K., and Zeilinger, A. *The Physics of Quantum Information* (Springer, 2000).

[5] Kimble, H. J. The Quantum Internet. *Nature* **453**, 1023 (2008).

[6] Simon, C., et al. Quantum Repeaters with Photon Pair Sources and Multimode Memories. *Phys. Rev. Lett.* **98**, 190503 (2007).

[7] Acin, A., et al. Device-Independent Security of Quantum Cryptography against Collective Attacks. *Phys. Rev. Lett.* **98**, 230501 (2007).

[8] Kwiat, P. G., et al. New High-Intensity Source of Polarization-Entangled Photon Pairs. *Phys. Rev. Lett.* **75**, 4337 (1995).

[9] Scarani, V., Riedmatten, H. De, Marcikic, I., Zbinden, H., and Gisin, N. Four-photon correction in two-photon bell experiments. *The European Physical Journal D-Atomic, Molecular, Optical and Plasma Physics* **32**, 129 (2005).

[10] Wang, X. L., et al. Experimental Ten-Photon Entanglement. *Phys. Rev. Lett.* **117**, 210502 (2016).

[11] Pan, J. W., et al. Multiphoton entanglement and interferometry. *Rev. Mod. Phys.* **2012**, 072501 (2012).

[12] Benson, O., Santori, C., Pelton, M., and Yamamoto, Y. Regulated and Entangled Photons from a Single Quantum Dot. *Phys. Rev. Lett.* **84**, 2513 (2000).

[13] Young, R. J., et al. A semiconductor source of triggered entangled photon pairs. *New J. Phys.* **8**, 29 (2006).

[14] Akopian, N., et al. Entangled Photon Pairs from Semiconductor Quantum Dots. *Phys. Rev. Lett.* **96**, 130501 (2006).

[15] Muller, A., Fang, W., Lawall, J. and Solomon, G S. Creating polarization-entangled photon pairs from a semiconductor quantum dot using the optical Stark effect. *Phys. Rev. Lett.* **103**, 217402 (2009).

[16] Müller, M., Bounouar, S., Jöns, K. D., Gläss, M. and Michler, P. On-demand generation of indistinguishable polarization-entangled photon pairs. *Nat. Photon.* **8**, 224 (2014).

[17] Chung, T. H., et al. Selective carrier injection into patterned arrays of pyramidal quantum dots for entangled photon light-emitting diodes. *Nat. Photon.* **10**, 782 (2016).

[18] Orieux, A., Versteegh, M. A. M., Jöns, K. D. and Ducci, S. Semiconductor devices for entangled photon pair generation: a review. *Rep. Prog. Phys.* **80**, 076001(2017).

[19] Huo, Y. H., Rastelli, A. and Schmidt, O . G. Ultra-small excitonic fine structure splitting in highly symmetric quantum dots on GaAs (001) substrate. *Appl. Phys. Lett.* **102**,152105 (2013).

[20] Keil, R., et al. Solid-state ensemble of highly entangled photon sources at rubidium atomic transitions. *Nat. Commun.* **10**, 15501 (2017).

[21] Huber, D., et al. Highly indistinguishable and strongly entangled photons from symmetric GaAs quantum dots. *Nat. Commun.* **10**, 15506 (2017).

[22] Ding, X., et al. On-demand single photons with high extraction efficiency and near-unity indistinguishability from a resonantly driven quantum dot in a micropillar. *Phys. Rev. Lett.* **116**, 020401 (2016).

[23] Somaschi, N., et al. Near-optimal single-photon sources in the solid state. *Nat. Photon.* **10**, 340-345 (2016).

[24] He, Y.-M., et al. Deterministic implementation of a bright, on-demand single-photon source with near-unity indistinguishability via quantum dot imaging. *Optica* **4**, 802-808 (2017).

[25] Claudon, J., et al. A highly efficient single-photon source based on a quantum dot in a photonic nanowire. *Nat. Photon.* **4**, 174 (2010)

[26] Reimer, M. E., et al. Bright single-photon sources in bottom-up tailored nanowires. *Nat. Commun.* **3**, 737 (2012)

[27] Laucht, A., et al. A Waveguide-coupled On-Chip Single-Photon Source. *Phys. Rev. X* **2**, 011014 (2012).

[28] Arcari, M., et al. Near-unity coupling efficiency of a quantum emitter to a photonic crystal waveguide. *Phys. Rev. Lett.* **113**, 093603 (2014).

[29] Gschrey, M., et al. Highly indistinguishable photons from deterministic quantum-dot microlenses utilizing three-dimensional in situ electron-beam lithography. *Nat. Commun.* **6**, 7662 (2015).

[30] Davanco, M., Rakher, M. T., Schuh, D., Badolato, A. and Srinivasan, K., A circular dielectric grating for vertical extraction of single quantum dot emission. *Appl. Phys. Lett.* **99**, 041102 (2011).

[31] Sapienza, L., Davano, M., Badolato, A. and Srinivasan, K. Nanoscale optical positioning of single quantum dots for bright and pure single-photon emission. *Nat. Commun.* **6**, 7833 (2015).

[32] Dousse, A., et al. Ultrabright source of entangled photon pairs. *Nature* **466**, 217 (2010).

[33] Jöns, K. D., et al. Bright nanoscale source of deterministic entangled photon pairs violating Bells inequality. *Sci. Rep.* **7**, 1700 (2017).

[34] Chen, Y., Zopf, M., Keil, R., Ding, F. and Schmidt, O. G. Highly-efficient extraction of entangled photons from quantum dots using a broadband optical antenna. *Nat. Commun.* **9**, 2994 (2018).

[35] Liu, J., et al. Cryogenic photoluminescence imaging system for nanoscale positioning of single quantum emitters. *Rev. Sci. Instrum.* **88**, 023116 (2017).

[36] Chen, Y., et al. Wavelength-tunable entangled photons from silicon-integrated IIIV quantum dots. *Nat. Commun.* **7**, 10387 (2016).

[37] Trotta, R., et al. Wavelength-tunable sources of entangled photons interfaced with atomic vapors. *Nat. Commun.* **7**, 10375 (2016).

[38] D. Huber et al. Strain-tunable GaAs quantum dot: An on-demand source of nearly-maximally entangled photon pairs. *Phys. Rev. Lett.* 121, 033902 (2018).

[39] Jayakumar, H., et al. Time-bin entangled photons from a quantum dot. *Nat. Commun.* **5**, 4251 (2014).

[40] Stufler, S., et al. "Two-photon Rabi oscillations in a single $In_xGas_{1-x}A/GaAs$ quantum dot," *Phys. Rev. B* **73**, 125304 (2006).

[41] Kaniber, M., et al. Efficient and selective cavity-resonant excitation for single photon generation. *New J. Phys.* **11**, 013031 (2009).

[42] Stevenson, R. M., et al. Evolution of Entanglement Between Distinguishable Light States. *Phys. Rev. Lett.* **101**, 170501 (2008).

[43] Ward, M. M., et al. Coherent dynamics of a telecom-wavelength entangled photon source. *Nat. Commun.* **5**, 3316 (2014).

[44] Hudson, A. J., et al. Coherence of an Entangled Exciton-Photon State. *Phys. Rev. Lett.* **99**, 266802 (2007).

[45] Duan, L. M., Lukin, M. D., Cirac, J. I. and Zoller, P. Long-distance quantum communication with atomic ensembles and linear optics. *Nature* **414**, 413 (2001).

[46] Santori, C., Fattal, D., Vuckovic, J., Solomon, G. S. and Yamamoto, Y. Indistinguishable photons from a single-photon device. *Nature* **419**, 594 (2002).

[47] Liu, J., et al., Single Self-Assembled InAs/GaAs Quantum Dots in Photonic Nanostructures: The Role of Nanofabrication. *Phys. Rev. Appl.* **9**, 064019 (2018).

[48] Kaldewey, T., et al. Coherent and robust high-fidelity generation of a biexciton in a quantum dot by rapid adiabatic passage. *Phys. Rev. B* **95**, 161302(R) (2017).

[49] Iles-Smith, J., McCutcheon, D. P. S., Nazir, A., and Mork, J.,

Phonon scattering inhibits simultaneous near-unity efficiency and indistinguishability in semiconductor single-photon sources. *Nat. Photon.* **11**, 521 (2017).

[50] Pathak, P. K. and Agarwal, G. S. Quantum random walk of two photons in separable and entangled states. *Phys. Rev. A* **75**, 032351 (2007).

[51] Prilmüller, M., et al. Hyperentanglement of Photons Emitted by a Quantum Dot. *Phys. Rev. Lett.* **121** 110503 (2018).

[52] Olbricha, F., et al. Polarization-entangled photons from an InGaAs-based quantum dot emitting in the telecom C-band. *Appl. Phys. Lett.*, **111**, 133106 (2017).

[53] Huwer, J., et al. Quantum-Dot-Based Telecommunication-Wavelength Quantum Relay. *Phys. Rev. Appl.* **8**, 024007 (2017).

[54] Li, Q., Davanço, M. and Srinivasan, K. Efficient and low-noise single-photon-level frequency conversion interfaces using silicon nanophotonics. *Nat. Photon.* **10**, 406 (2016).

[55] Gao, W. B., et al. Quantum teleportation from a propagating photon to a solid-state spin qubit. *Nat. Commun.* **11**, 2744 (2013)

**Acknowledgements**
We acknowledge R. Trotta, X. Yuan, H. Huang, M. Reindl, D. Huber and Y. Huo for very fruitful discussions. We are greatful to the financial supports from the National Key R&D Program of China (2016YFA0301300, 2018YFA0306100), the National Natural Science Foundations of China (91750207, 1133405, 11674402, 11761141015, 11761131001, 11874437), Guangzhou Science and Technology project (201607020023, 201805010004), the Natural Science Foundations of Guangdong (2018B030311027, 2016A030312012), and the Austrian Science Fund (FWF): P29603.

**Author Contributions**
R. B. S, J. T. L and X. H. W conceived the nanostructure and its fabrication strategy. J. L designed the measurement scheme. R. B. S and K. S contributed to the structure simulations. S. F. CdS and Y. Y grew the quatum dot wafers. R. B. S, B. M. Y, J. T. L and J. L fabricated the devices. Y. M. W, R. B. S, B. M. Y and J. L characterized the devices. J. I. S performed the indistinguishability calculation. J. L, Y. M. W, and R. B. S analyzed the data. J. L wrote the manuscript with inputs from all authors. J. L, A. R and X. H. W supervised the project.

**Competing financial interests**
The author declare that they have no competing financial interests.

**Data availability statement**
The data that support the plots within this paper and other findings of this study are available from the corresponding author upon reasonable request.

**Additional information**
**Supplementary information** is available in the online version of the paper.
**Reprints and permission information** is available online at www.nature.com/reprints.
**Correspondence and requests for materials** should be addressed to A. S, J. T, L or X. H. W.

## Methods

**Simulation**
The numerical simulaitons are carried out by means of finite-difference time-domain method, using a commercial software, Lumerical FDTD solutions. An electrical dipole is placed in the center of the CBR-HBR structure and six power monitors emcompassing the structure are employed to record power emitted by the dipole source. The sum power transmission normalized to that of the same source in homogeneous materials is calculated as the Purcell factor. The electric field record by the top monitor is used to calculate the far-field pattern by means of near-field to far-field projection. The collection efficiencies are extracted from the far-field distribution in 40 degree corresponding to N.A. of 0.65 (for further details see S.I. section II).

**Fabrication**
The epi-structure of the wafer is schematically shown in S.I. I. After cleaning with acetone and isopropanol, 220 nm $SiO_2$ layer and 100 nm Au layer are deposited on the wafer by inductively coupled plasma chemical vapor deposition (Oxford instruments, PlasmaPro System100 ICP180-CVD) and electronic beam evaporation (Wavetest, DE400) repectively. The wafer is bonded to a glass substrate via ultraviolet curing resist (Norland, NOA 61). After exposure, the wafer is placed in a 50 °C thermostat for 24 hours aging process to get an optimized performance. The original GaAs substrate is removed with phosphoric acid ($H\_2PO_4$:$H_2O_2$:$H_2O$ = 1:1:1 volume) for 1.5 hour and selective etching solution (citric acid:$H_2O_2$ = 3:1 volume) until stopping at the sacrificial layer. The $Al_{0.8}Ga_{0.2}As$ sacrificial layer is removed with 10% HF. The CBR-HBR structures are defined by an electron beam lithography(Vistec EBPG5000+ system). The alignment marks (10 nm Ti and 100 nm Au) are patterned with an electron beam lithography and a lift-off process. An Ar-$SiCl_4$ based dry etching process(Oxford instruments, PlasmaPro System 100 ICP180) is used to etch the GaAs structure.

**Two-photon resonant excitation**
A Ti-sapphire pulsed laser with a pulse duration of 120 fs and 79 MHz repetition rate is used to excited the QDs. In order to realize the two-photon resonant excitation scheme, the Ti-saphire laser is shaped by a home-made 4f-pulse shaper into a 8 ps pulse and spectrally tuned in the middle of the X and XX lines. The sample is excited by the optical pulses via an objective with a NA=0.65 and the emitted photon pairs are collected with the same objective. A notch filter is used to suppress the scattered laser background.

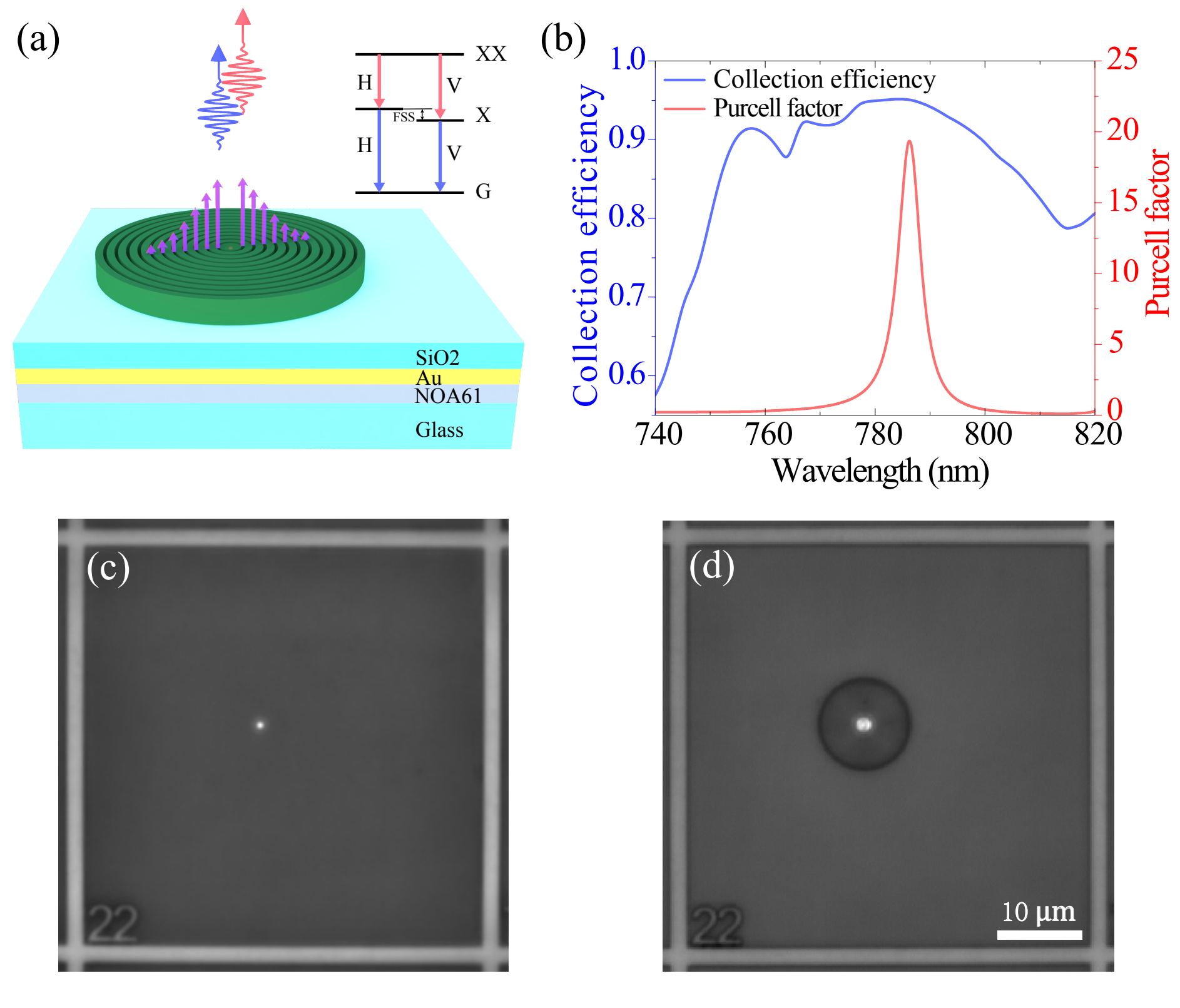
(a)
XX
H
V
FSS
X
H
V
G
SiO2
Au
NOA61
Glass
(b)
Collection efficiency
Purcell factor
Collection efficiency
Purcell factor
Wavelength (nm)
1.0
0.9
0.8
0.7
0.6
25
20
15
10
5
0
740
760
780
800
820
(c)
22
(d)
22
10 µm

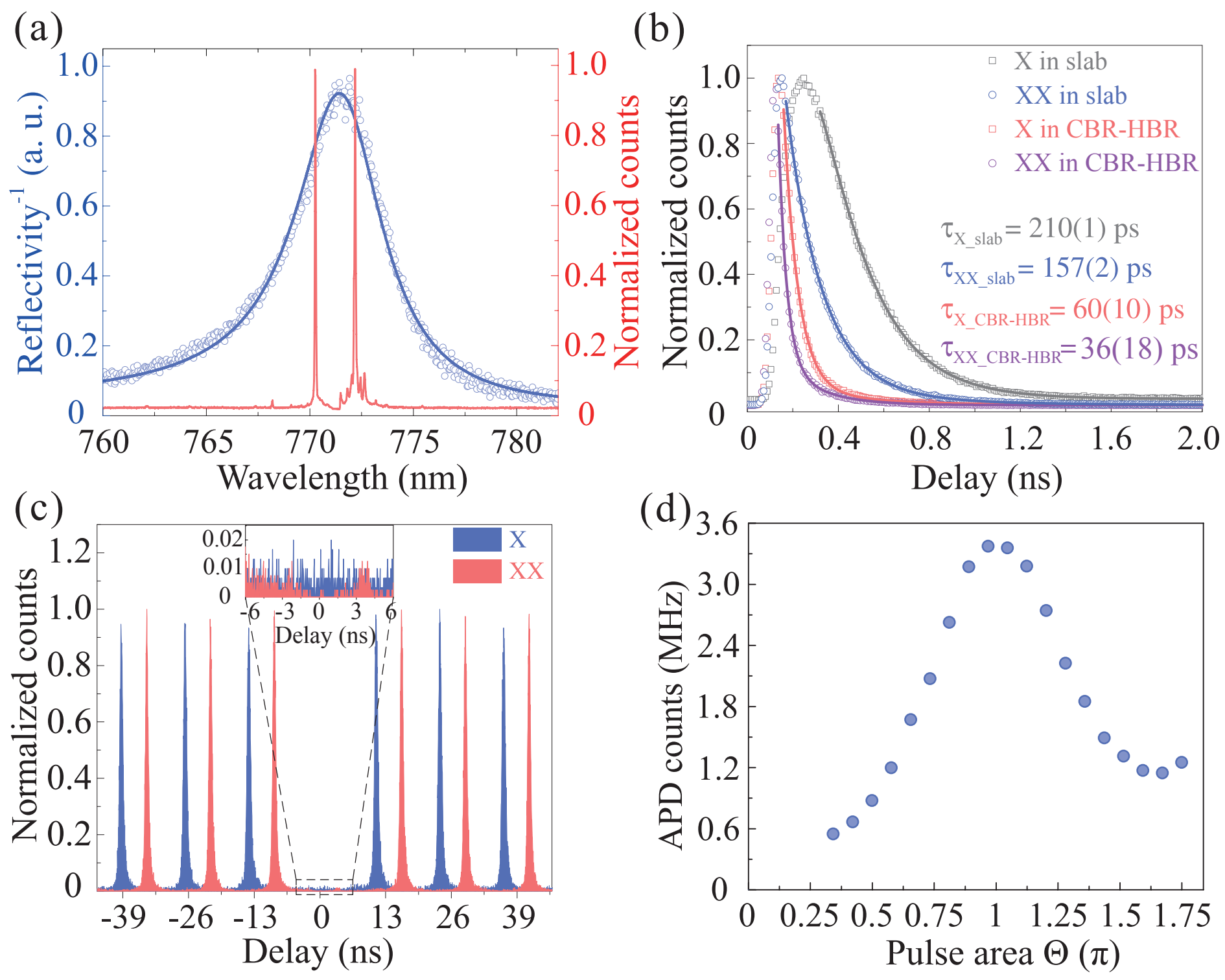
(a)
Reflectivity$^{-1}$ (a. u.)
Normalized counts
Wavelength (nm)
(b)
X in slab
XX in slab
X in CBR-HBR
XX in CBR-HBR
$\tau_{X\_slab}$ = 210(1) ps
$\tau_{XX\_slab}$ = 157(2) ps
$\tau_{X\_CBR-HBR}$ = 60(10) ps
$\tau_{XX\_CBR-HBR}$ = 36(18) ps
Normalized counts
Delay (ns)
(c)
X
XX
Normalized counts
Delay (ns)
(d)
APD counts (MHz)
Pulse area Θ (π)

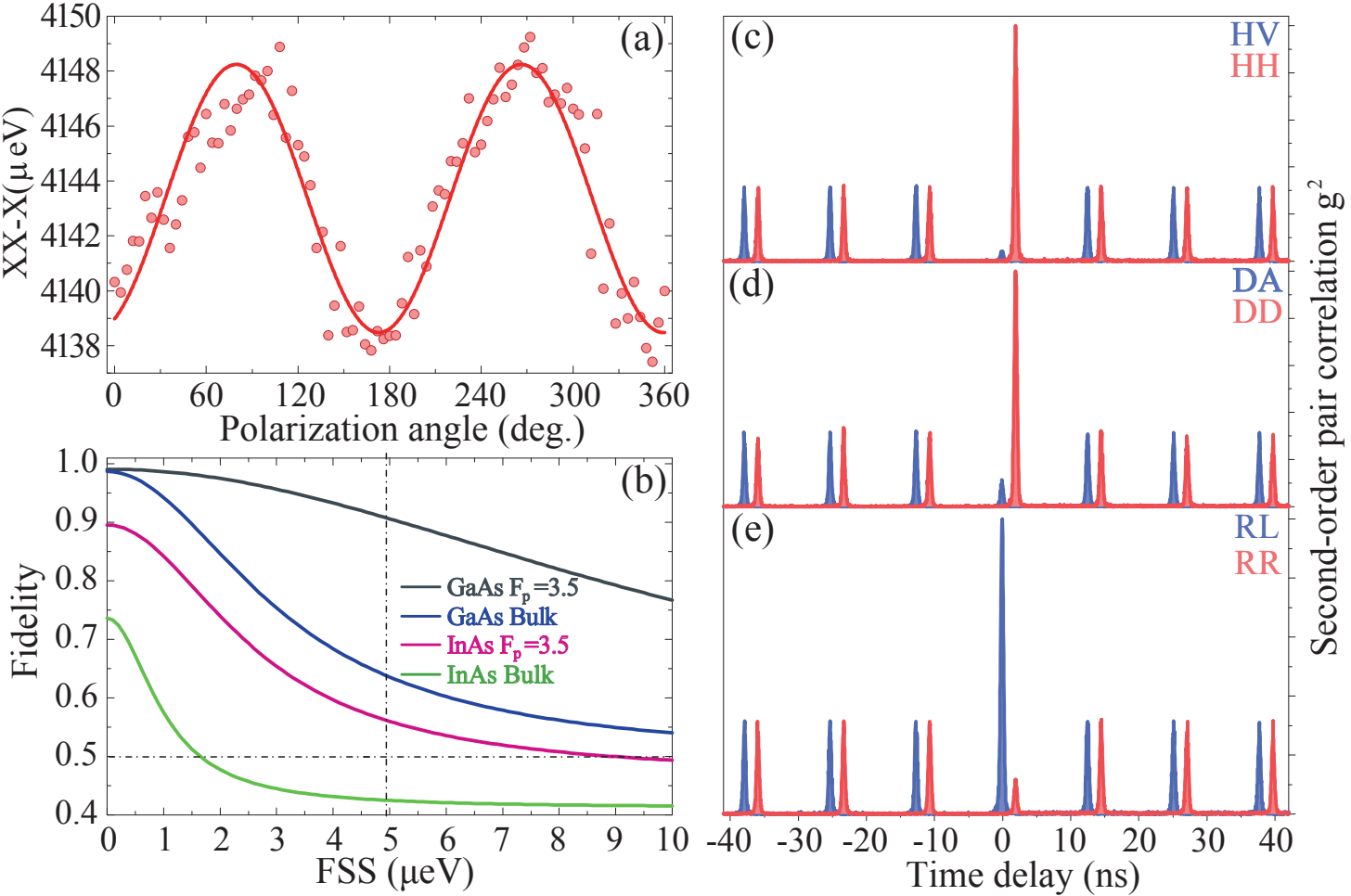
(a)
XX-X(μeV)
4150
4148
4146
4144
4142
4140
4138
0
60
120
180
240
300
360
Polarization angle (deg.)
(b)
Fidelity
1.0
0.9
0.8
0.7
0.6
0.5
0.4
GaAs F_p=3.5
GaAs Bulk
InAs F_p=3.5
InAs Bulk
0
1
2
3
4
5
6
7
8
9
10
FSS (μeV)
(c)
HV
HH
(d)
DA
DD
(e)
RL
RR
-40
-30
-20
-10
0
10
20
30
40
Time delay (ns)
Second-order pair correlation g^2

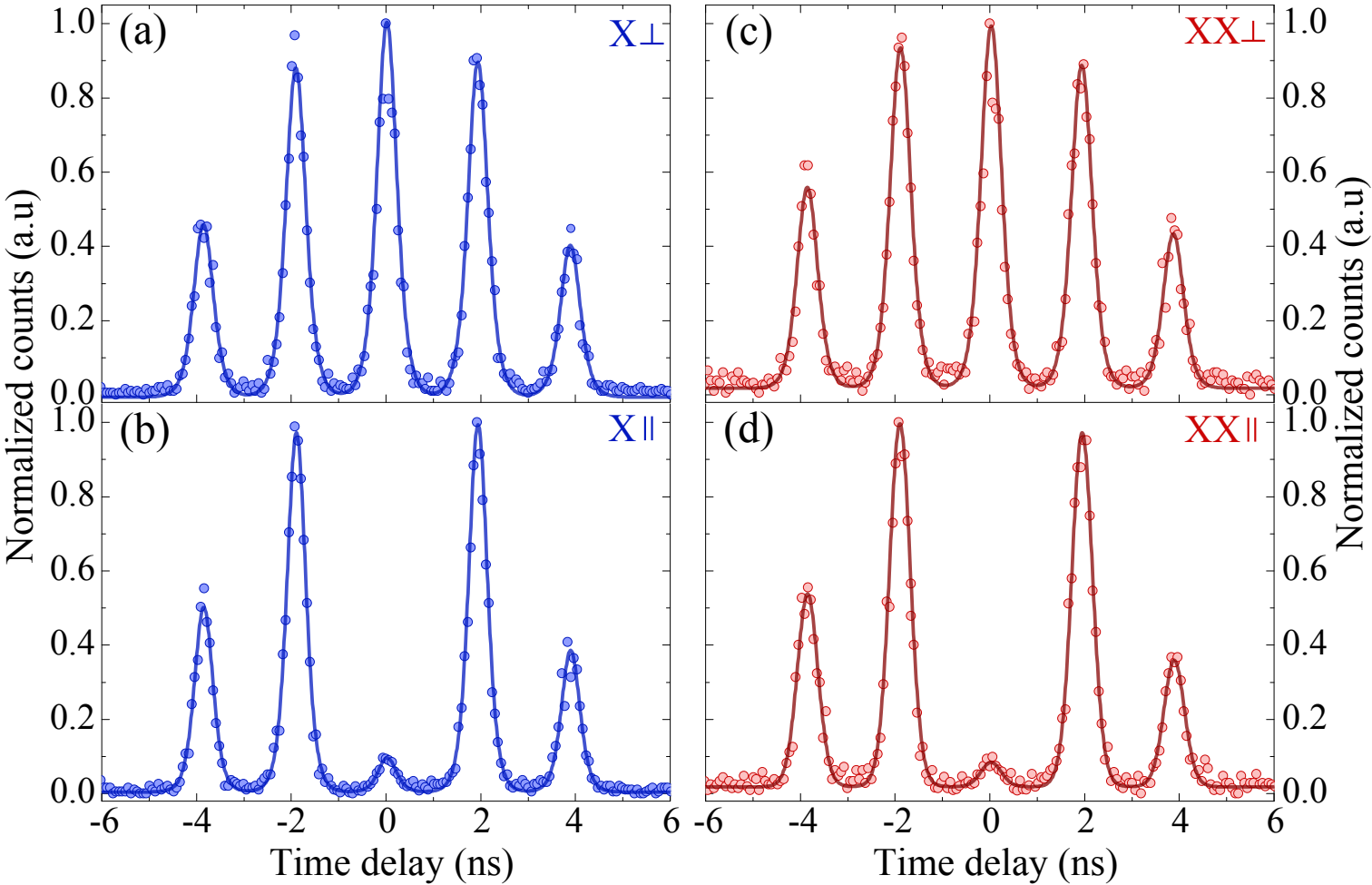
(a)
X⊥
(b)
X∥
(c)
XX⊥
(d)
XX∥
Normalized counts (a.u)
Normalized counts (a.u)
Time delay (ns)
Time delay (ns)
0.0
0.2
0.4
0.6
0.8
1.0
-6
-4
-2
0
2
4
6

# Supplementary Information to "A solid-state entangled photon pair source with high brightness and indistinguishability"

Jin Liu,[*] Rongbin Su,[*] Yuming Wei, Beimeng Yao, Saimon Filipe Covre da Silva, Ying Yu, Jake Iles-Smith, Kartik Srinivasan, Armando Rastelli,[†] Juntao Li,[†] and Xuehua Wang[†]

(Dated: December 16, 2018)

## I. DROPLET QUANTUM DOT GROWTH AND CHARACTERIZATION

The quantum dot (QD) samples are grown on semi-insulating GaAs (001) substrates by a solid source molecular beam epitaxy (Veeco GENxplor system). A sketch of the heterostructure is shown in Fig. S1(a). It consisted of a 500-nm-thick sacrificial $Al_{0.8}Ga_{0.2}As$ layer (not to scale), a 4-nm-thick GaAs layer, a 140-nm-thick $Al_{0.4}Ga_{0.6}As$ layer and a 4-nm-thick GaAs capping layer from the bottom to the top. A layer of low-density ($\sim 10^{-6} - 10^{-7} cm^{-2}$) GaAs QDs are embedded in the middle of the $Al_{0.4}Ga_{0.6}As$ layer by introducing local droplet etching process as previous reported[S1]. In brief, the nanoholes are obtained by depositing 0.5 monolayer of aluminum droplets on the $Al_{0.4}Ga_{0.6}As$ surface at a substrate temperature of 640 °C followed by 5 min annealing under $As_2$ flux. The nanoholes are then overgrown with 2 nm GaAs followed by 5 min annealing. Atomic force microscopy (AFM) of a representative nanohole (see Fig. S1(b)) reveals a GaAs QD with a width of about 60 nm, a height of about 5.6 nm and a highly-symmetric shape. Such a shape symmetry is directly correlated to the excitonic fine structure splitting that is of fundamental importance for the generation of entangled photons.

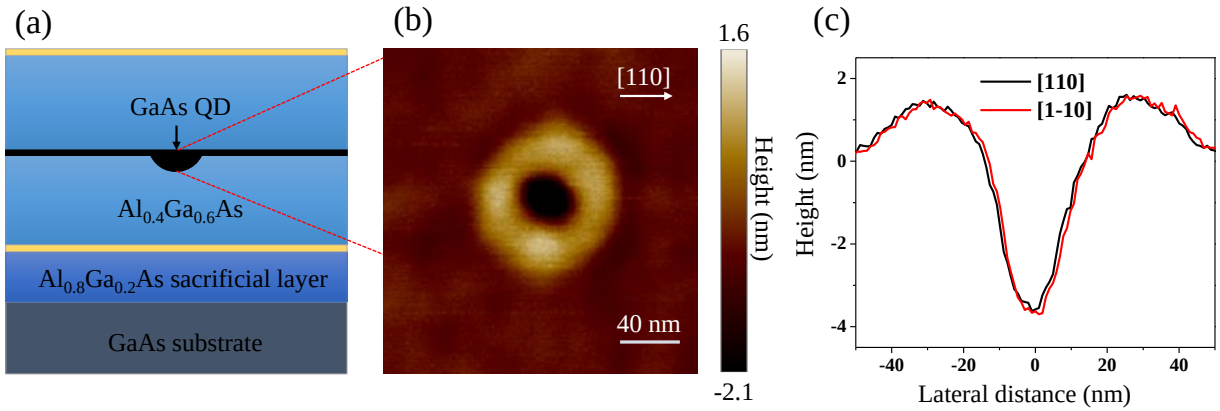


FIG. S1: **Droplet growth of QDs.** (a) Sketch of the QD sample. (b) An AFM image of an etched nanohole in the AlGaAs layer. (c) The line scans across the nanohole, showing symmetric profiles along both [110] and [1-10] directions.

## II. COMPARISION BETWEEN THE CBR-HBR AND THE SUSPENED CBG

Figure S2 shows the fabrication process of our new suspended circular Bragg grating (CBG), previously studied in Ref. S2,S3, and a comparison of collection efficiency between our new CBR-HBR and the suspended CBG. The fabrication process of the suspended CBG doesn't require membrane transfer, wafer bonding and substrate removal processes, and is thus easier to implement, as shown in Fig.S2(b). The collection efficiency has been improved from ∼50% to >90% by suppressing the backside photon leakage with the CBR-HBR structure, shown in Fig. S2(c). However, in addition to the efficiency limitation, we have found that the suspended CBG geometry has some challenges with respect to robustness and reproducibility, as it relies upon achieving a precise etch depth for the circular trenches (variations in the etch depth influence the resonance frequency, Purcell enhancement, and collection efficiency). Our new CBR-HBR geometry, with fully etched trenches (that stop at the underlying $SiO_2$ layer) is both more mechanically robust and repeatable.

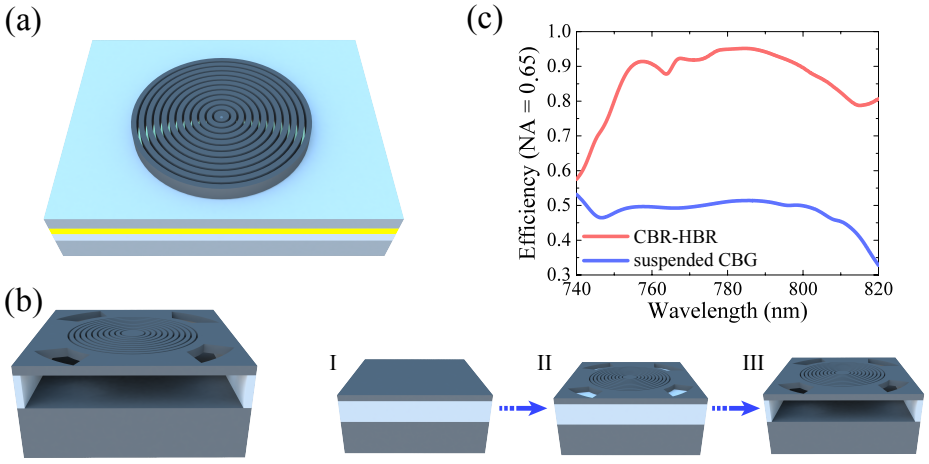


FIG. S2: **Comparision between the CBR-HBR and the suspended CBG.** (a) Schematic of CBR-HBR. (b) The schematic of the suspended CBG and its fabrication process. II: transfering the pattern into GaAs via E-beam lithography and dry etching. III: releasing the membrane via a selective wet etching process. (c) Comparison of the collection efficiency between CBR-HBR and suspended CBG.

## III. NUMERICAL SIMULATIONS

Our design of the CBR-HBR starts with a 1D grating (radial section of CBR) made of $Al_{0.4}Ga_{0.6}As$, sitting on a $SiO_2$ buffer layer ($n = 1.45$) and immersed in air ($n = 1$), see Fig. S3(a). A waveguide TE mode excitation is launched to the 1D grating and the band edge around 820 nm can be identified, shown in Fig. s2(a). The photons with wavelength in the reflection band will be scattered upwards/downwards in the grating area, which is attributed to the second-order Bragg condition. Once the band edge is identified with the 1D model, we use a 3D finite difference time domain (FDTD) simulation to design the cavity resonance of the CBR placed on $SiO_2$ and without an Au reflector, by varying the radius (R) of the central $Al_{0.4}Ga_{0.6}As$ disk, shown in Fig. S3(b). The cavity resonances shift systematically to the longer wavelength with the increase of the cavity length (i.e. the diameter of the central disk). Finally, we add an Au reflector underneath and tune the thickness of the $SiO_2$ spacer to reflect all the down-leaking photons back to the CBR area. Figure S2(c) shows the XZ cross-section of the electric field in the CBR-HBR, in which most of the emitted photons are guided upwards with a small divergence angle. The small divergence angle of the upwards emission is further confirmed by the simulated far-field pattern, shown in the inset of Fig. S3(c).

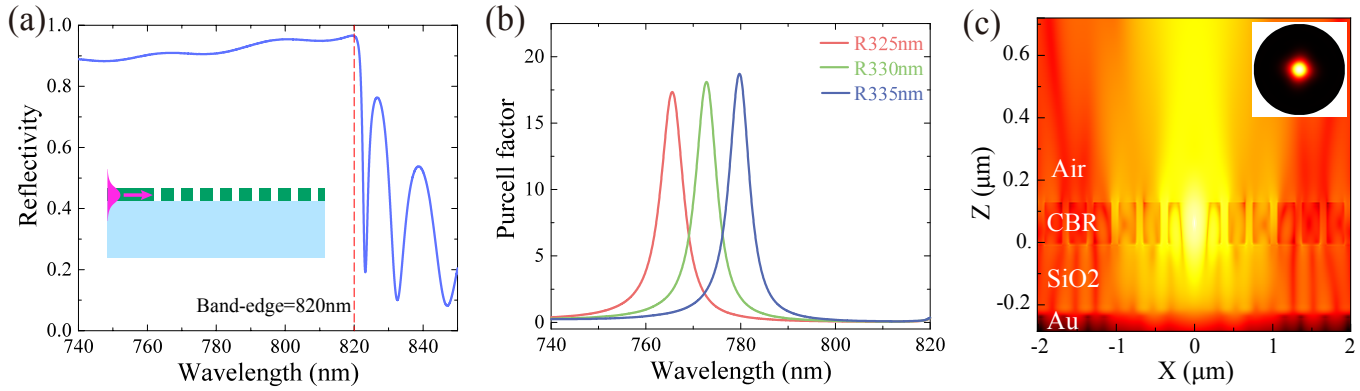


FIG. S3: **Design of the CBR-HBR.** (a) Reflection band of a 1D grating structure. (b) Purcell factors for the CBRs with different cavity lengths. (c) The XZ cross-section of the simulated electric field distribution in the CBR-HBR. Inset is the calculated far-field pattern.

## IV. DEVICE FABRICATION

The fabrication flow is schematically shown in Fig. S4. Our process starts with depositions of 220 nm $SiO_2$ and 100 nm Au on top of the QD wafer. Then the top surface of the III-V wafer is bonded to a transparent quartz substrate with NOA61 via an ultra-violent curing process (Fig. S4(a)). Citric- and HF-acids are used to selectively remove the GaAs substrate and the $Al_{0.8}Ga_{0.2}As$ sacrificial layer. After the wet etching processes, the QD-containing $Al_{0.4}Ga_{0.6}As$ layer is sitting on top of $SiO_2$ with a gold reflector (Fig. S4(b)). We then fabricate the alignment marks for QD positioning by using an electron beam lithography and lift-off process (Fig. S4(c)). Once the alignment marks are on the chip, we apply the fluorescence imaging technique to extract the spatial positions of QDs with respect to the alignment marks (Fig. S4(d)). The PL-spectra for the targeted QDs are also taken, in order to design the cavity resonance of the CBRs. With the spatial and spectral information of each targeted QD, we fabricated surrounding CBR structures with carefully engineered resonances by an aligned E-beam lithography and a chlorine-based dry etch process (Fig. S4(e)). A scanning electron microscope (SEM) image of the fabricated device is shown in Fig. S4(f).

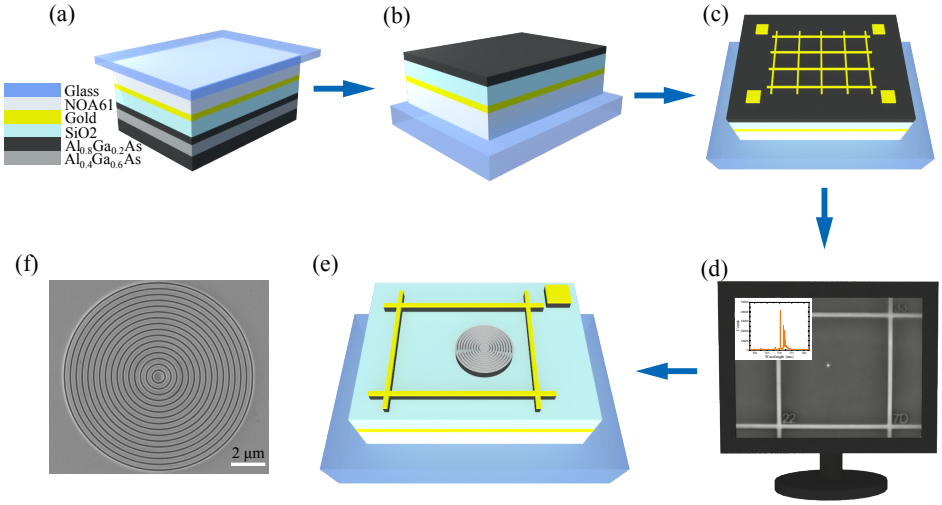


FIG. S4: **Fabrication of the CBR-HBR.** Fabrication process of the CBR-HBR is schematically shown. (a) 220 nm $SiO_2$ and 100 nm Au are deposited on a $Al_{0.4}Ga_{0.6}As$ (containing GaAs droplet QDs) thin film and this side is glued to a quartz substrate with NOA61 by ultraviolet curing. (b) The GaAs substrate and $Al_{0.8}Ga_{0.2}As$ sacrificial layer are removed by citric- and HF-acid selective etching respectively. (c) The Au markers are defined by the E-beam lithography, metal deposition and lift-off technologies. (d) The PL-images and spectra of the targeted QDs are taken to extract the spatial and spectral information for the CBR-HBR fabrication. (e) CBR structures with engineered cavity resonances are fabricated around each targeted QDs via an aligned E-beam lithography and chlorine-based dry etching. (f) A SEM image of the fabricated CBR-HBR. The device consists of a central disk with 660 nm diameter, surrounding circular gratings with a period of 330 nm and fully-etched trenches with a width of 90 nm.

## V. SCHEMATICS OF THE SETUP FOR OPTICAL CHARACTERIZATIONS

The setup for optically characterizing the entangled sources is schematically shown in Fig. S5. We use a confocal $\mu$-PL microscope, shown in Fig. S5(a), to probe the photons emitted by QDs in CBR-HBRs located in a 3.2 K closed-circle cryostat. Half of the emitted photons go to the EMCCD for fluorescence imaging (for QD positioning process) via a 50/50 splitter. The other half of the emitter signal is guided to either spectrometer (Fig. S5(b)) or Hong-Ou-Mandel (HOM) (Fig. S5(c)) interferometer or the entanglement section (Fig. S5(d)) via flip mirrors. In the spectrometer section, the PL-spectra and lifetimes are measured by switching between the CCD and APD exits of the monochromator. In the HOM interferometer, the emitted photons are firstly filtered by a volume grating and projected to the horizontal polarization. A 1.9 ns delay in one arm of an unbalanced Mach-Zehnder interferometer (MZI) is set to match the delay time of the pump pulse (1.9 ns). We use a half-wave plate to set the co-polarized and cross-polarized configurations for the HOM intererence. For entanglement fidelity evaluation, the X and XX-photons are dispersed by the same volume grating and spatially separated by a right angle prism mirror before projecting to different polarization basis for cross-correlation measurements.

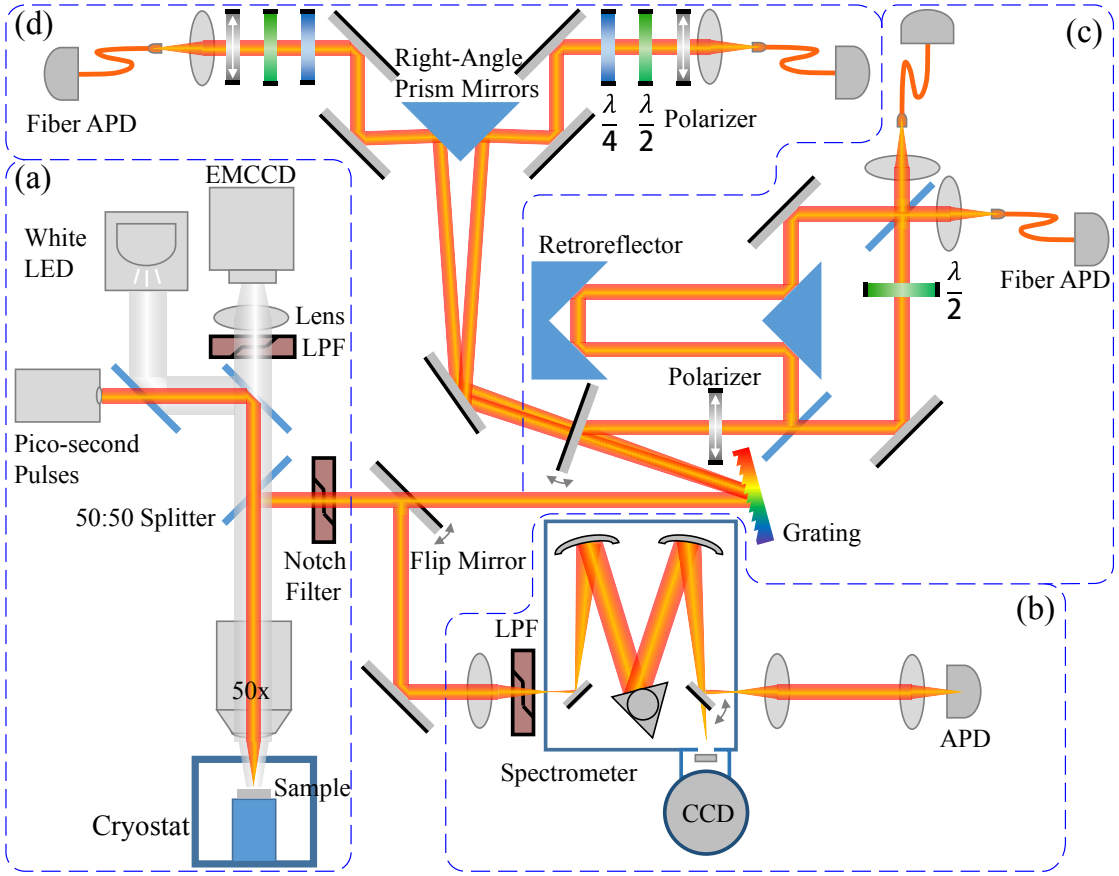


FIG. S5: **Schematic of the setup for optical characterizations.** (a) Confocal $\mu$-PL setup for QD fluorescence imaging. (b) Spectrometer for measuring QD PL-spectra, lifetimes and collection efficiency. (c) HOM interferometer for photon indistinguishability measurement. Second-order auto-correlations ($g^{(2)}(0)$) are also measured with this section by blocking one arm of the MZI. (d) Entanglement section for measuring the intensity cross-correlations between X and XX photons at different polarization basis.

## VI. CALIBRATION OF THE CAVITY MODES

In order to achieve pronounced Purcell effect in our devices, it is highly desirable to accurately control the cavity resonances and match them to the QD emissions. As the refractive index value we use in simulations could be different from the real values, particularly considering the cryogenic temperatures at which the devices operated, deviations of the observed cavity resonances from the designed ones are likely to be expected. Thus, we've carefully calibrated the cavity resonances of CBR-HBRs by fabricating a set of dummy structures with varied parameters. Fig. S6 shows the measured cavity resonances for the fabricated CBR-HBRs with different cavity lengths (the diameter of the central AlGaAs disks). The measured cavity resonance as well as the band edge systematically shift to the longer wavelength with the increase of the cavity length, which is very consistent with the simulation in Fig. S1(b). More specifically, ≈1 nm change in the cavity length gives rise to ≈1.2 nm shift in the cavity resonance. With these parameters, we are able to maximize the possibility of matching the cavity resonances to each of the individual QDs we have positioned.

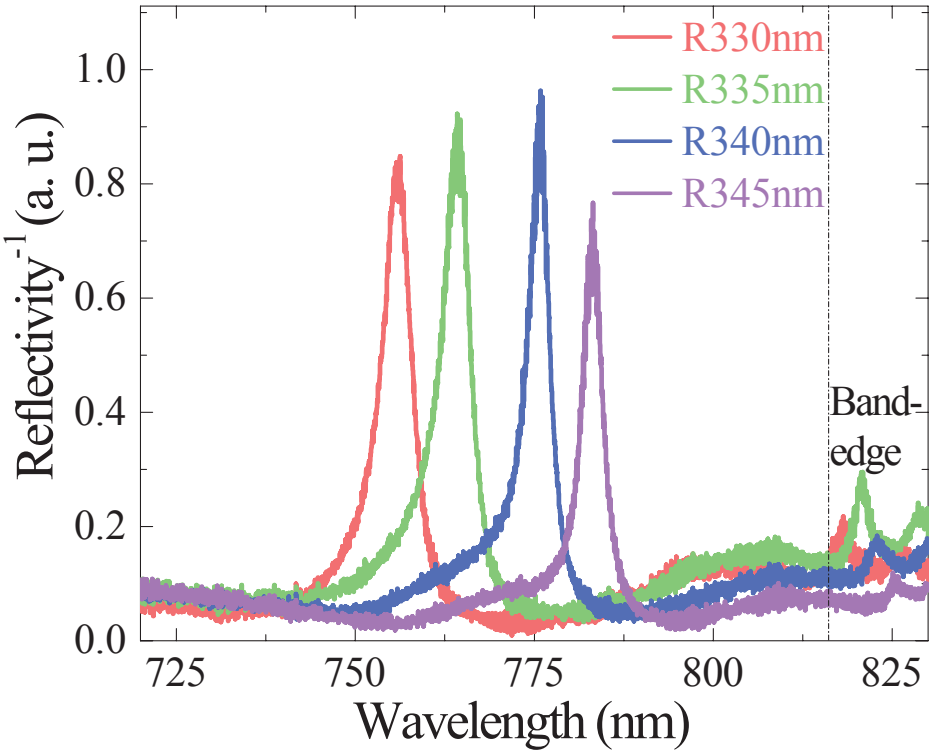


FIG. S6: **Calibration of the CBR-HBR cavity modes.** The measured cavity resonances of CBR-HBRs with different cavity lengths. The band edges at ≈820 nm are highlighted.

## VII. COLLECTION EFFICIENCY ESTIMATION

The system efficiency ($\xi \sim 0.07$) from the cryostat window to the APD after the monochromator (Fig. S6(a,b)) is carefully calibrated by sending a CW laser at the QD wavelength through the system. It consists of a cryostat window (transmission:$0.95 \pm 0.02$), a microscope objective (transmission:$0.90 \pm 0.02$), a 50/50 beam splitter (transmission:$0.53 \pm 0.02$), a notch filter (transmission:$0.90 \pm 0.02$), mirrors (transmission:$0.92 \pm 0.02$), a 400 nm long-pass filter (transmission:$0.94 \pm 0.02$), a monochromator (transmission:$0.30 \pm 0.05$) and a APD (quantum efficiency:$0.66 \pm 0.03$). Due to the high count rates in the APD, a correct factor of 1.25 is obtained by taking into account the APD dead time $\sim$60 ns: $R_{actual} = R_{measured}/(1 - R_{measured} * T)$, in which $R_{actual}$ is the real photon counts, $R_{measured}$ is the measured photon count rate (3.4 MHz) and $T$ is the dead time of the APD (60 ns). The XX preparation rate $\eta_{XX}$ ($\sim 0.9$) is obtained from the ratio of X photon count rate at $\pi$ pulse under TPE and the count rate under above band excitation (405nm) at the saturation power.

## VIII. CALCULATION OF THE ENTANGLEMENT FIDELITY

We follow the work by Hudson *et al*[S4] to model the entanglement fidelities for QDs in different material with varied Purcell factors as a function of the fine structure splitting (FSS). Given the fact that the effect of cross-dephasing can be safetly neglected[S4], the entanglement fidelity can be wrtitten as:

$$f = \frac{1}{4}(1 + g^{'}_{H,V} + \frac{2kg^{'}_{H,V}}{1+x^2}) \tag{1}$$

where $g^{'}_{H,V} = 1/(1 + T_1/T_{ss})$, $x = \frac{g^{'}_{H,V} s T_1}{\hbar}$ with $T_{SS}$ the spin scattering time, $T_1$ the exciton decay time, the FSS (denoted by s) and the fraction $k = 1 - g^{(2)}(0)$ of photons emitted exclusively by the QD. With the measured exciton lifetime $T_1$ and the value of $g^{(2)}(0)$ to estimate k, the only unknown paramter in Equation 1 is the spin-scattering time $T_{ss}$. As in Ref. S4, we assume the the $T_{ss}$ is dominated by the Fermi-contact interaction between the confined electron and the nuclear spins[S5] while the heavy-hole dephasing due to the dipole-dipole interaction[S5,S6] is too weak to be considered. We take the values from literature ($T_{ss} =$ 15 ns[S7] for GaAs QDs and $T_{ss} = 1.9$ ns[S8] for InGaAs QDs) to plot the entanglement fidelities of QDs in different material with varied Purcell factors. While the measured entanglement fidelity is the very close to the calculated number, a small discrenpancy could exist due to variation of the $T_{ss}$ between the individual QDs. In addition, recent works[S9] tentatively attribute the residual dephasing to spin scattering with charges in the surrounding of the QDs.

## IX. STRAIN-TUNABLE CBR-HBR

Moving forwards to bright sources with near-unity entanglement fidelity, it is highly desirable to controll the FSS of the QDs in CBR-HBR. Figure S7 shows the design of the strain-tunable CBR-HBR, in which a CBR-HBR is directly sitting on top of $0.72Pb(Mg_{1/3}Nb_{2/3})O_3 0.28PbTiO_3$ (PMN-PT) chip instead of a transparent quartz substrate. By applying a voltage via the Au layers below and above the PMN-PT chip, the FSS of QDs in CBR-HBR can be efficiently elminated via the strain induced by the PMN-PT actuator. The development of CBR-HBR with strain-tunable function is currently in progress.

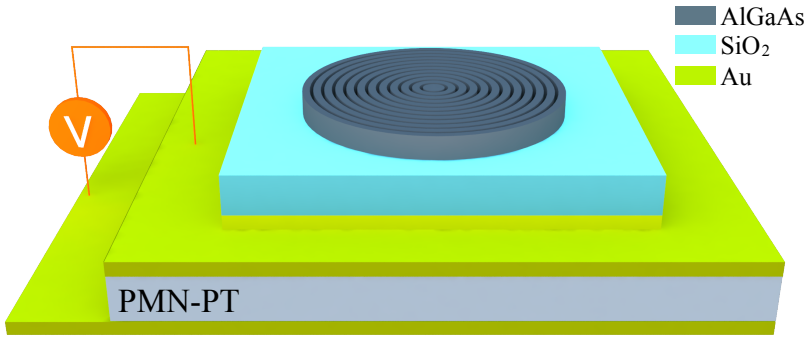


FIG. S7: **Strain-tunable CBR-HBR.** The schematic of the strain-tunable CBR-HBR.

## X. ESTIMATION OF THE LIMIT OF PHOTON INDISTINGUISHABILITY WITH MICROSCOPIC PHONON SCATTERING MODEL

As demonstrated in Ref. S10, the indistinguishability of QD emitters is limited by electron-phonon interactions, and resultant phonon sidebands present in the emission spectrum from QDs. In this section we estimate the upper bound on the indistinguishability for the source presented in the main manuscript, accounting for the leading order electron-phonon interactions[S11] and neglecting any other dephasing processes (e.g. charge noise), using typical material parameters for GaAs.

To calculate the photon indistinguishability using the formalism presented in S10, we first need to establish suitable electron-phonon parameters. The interaction between an open quantum system and its environment is fully specified by the spectral density $J(\omega) = \sum_k |g_k|^2 \delta(\omega - \omega_k)$, where $g_k$ is the coupling strength between the system and the $k^{th}$ mode of the phonon environment, and $\omega_k$ is the frequency of the phonon with wavevector $k$. This function quantifies the coupling strength to the system weighted by the density of states of the phonon environment. If we assume a spherically symmetric QD, where the electrons and holes are confined in a spherically symmetric parabolic potential, then the spectral density takes the analytic form[S12]:

$$J(\omega) = \alpha\omega^3 e^{-\omega^2/\omega_c^2} \tag{2}$$

where the phonon interaction is now characterised by two parameters: The electron phonon coupling strength, $\alpha$, depends purely on material parameters:

$$\alpha = \frac{(D_e - D_h)^2}{4\pi^2\hbar\rho c_s^5} = 0.025 \text{ ps}^2$$

where we have introduced the deformation potential coupling for electrons, $D_e = -15.93$ eV, and holes, $D_h = -15.93$ eV[S13]. The additional parameters are the material density $\rho = 5.317$ g cm$^{-3}$ and speed of sound $c_s = 4.73 \times 10^5$ cm s$^{-1}$ in Ref. S14.

The cut-off frequency, $\omega_c$, depends on the size of the QD, $\omega_c = \sqrt{2}c_s/d = 1.195$ ps$^{-1}$ where $d$ is the confinement length for the exciton. Through the AFM analysis, we can estimate that the QD has a diameter of $\sim 60$ nm and height 4.6 nm. We take the smallest length to have the dominant impact on the excitonic wavefunction, leading to a cutoff frequency $\omega_c = 1.195$ ps$^{-1}$.

Using these parameters we can now use the formalism presented in Ref. S10 to calculate the indistinguishability. In the absence of a cavity, and with no spectral filtering, this is related to the Frank-Condon factor $B = \exp\left(-\frac{1}{2}\int_0^\infty \omega^{-2} J(\omega)\coth(\omega/2k_bT)d\omega\right) = 0.98$, where $T$ is the inverse temperature of the phonon envrionment and $k_b$ is Boltzmann's constant. The square of this parameter quantifies the probability of light being emitted through the ZPL rather than the phonon sideband. The indistinguishability of the light from the emitter is then determined by the probability of two photons being emitted through the ZPL, that is $I = B^4 = 0.936$.

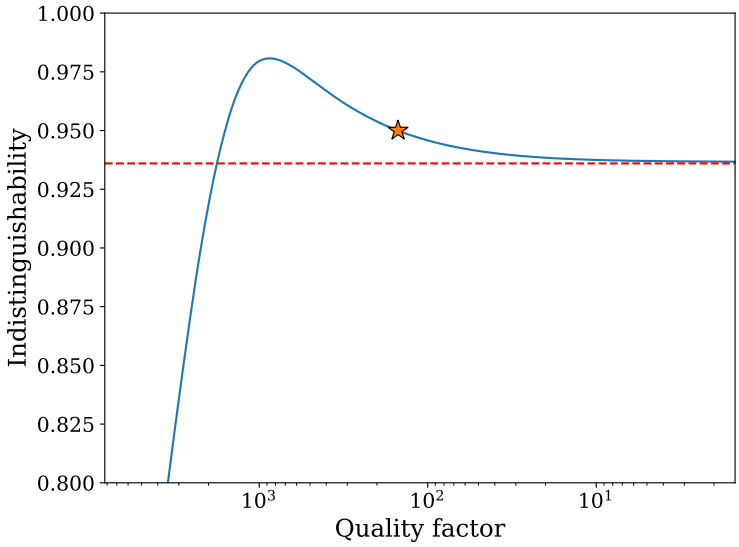


FIG. S8: Indistinguishability for the light-matter coupling strength $g = 149$ GHz as a function of cavity quality factor. The red dashed line is the indistinguishability in the absence of a cavity. The current quality factor $Q$-factor $= 150$ with a corresponding indistinguishability of 0.95.

This simple picture is complicated when a cavity is present, where the energy scale of the cavity has a non-trivial influence on the phonon environment.

We account for this effect using the well established polaron master equation formalism[S10,S15,S16], which uses a unitary transformation to incorporate important environmental effects into the system Hamiltonian. This constitutes an optimised basis for perturbation theory, allowing strong coupling andd non-Markovian behaviour to be captured, while keeping the intuitive and computationally simple master equation description.

For a detailed account on the derivation of the polaron master equation, we refer the reader to the supplementary information of Ref. S10.

Fig. S8 shows the indistinguishability as a function cavity $Q$-factor in the presence of electron-phonon interactions using the parameters derived above. This figure shows the presence of two competing processes. For cavities with low to intermediate Q-factors, increasing the Q-factor acts to increase the indistinguishability, this can attributed to two properties of the cavity: 1) the natural filtering that occurs due to the line shape of the cavity; 2) the increased emission rate due to the Purcell effect. As can be seen from Fig. S8, the indistinguishability monotonically increases until Q$\sim$1300.

After this point the indistinguishability rapidly drops, heralding a transition into the strong coupling regime. The cavity and QD now coherently exchange the excitation, undergoing Rabi oscillations. Each time the QD is excited, the lattice of the host material is displaced due to a change in charge configuration in the QD, leading to an emission of phonons when the exciton recombines and the photon is emitted back into the cavity. This leads to a degradation of the indistinguishability, as phonon emission leads to dephasing.

From Fig. S8 we can identify a an upper bound for the indistinguishability of $I = 0.98$ for the GaAs phonon parameters, this occurs for a $Q$-factor$= 1373$. We can also ask what is the upper bound for the indisinguishability for the bright single photon source presented in the main manuscript. For a $Q = 150$, the indistinguishability is bounded from above $I \leq 0.95$. This value is highlighted in Fig. S8 by the star.

## XI. ENTANGLEMENT AND INDISTINGUISHABLITY OF DEVICE 4

The data of entanglement fidelity and indistinguishability of device 4 are presented in Fig. S9.

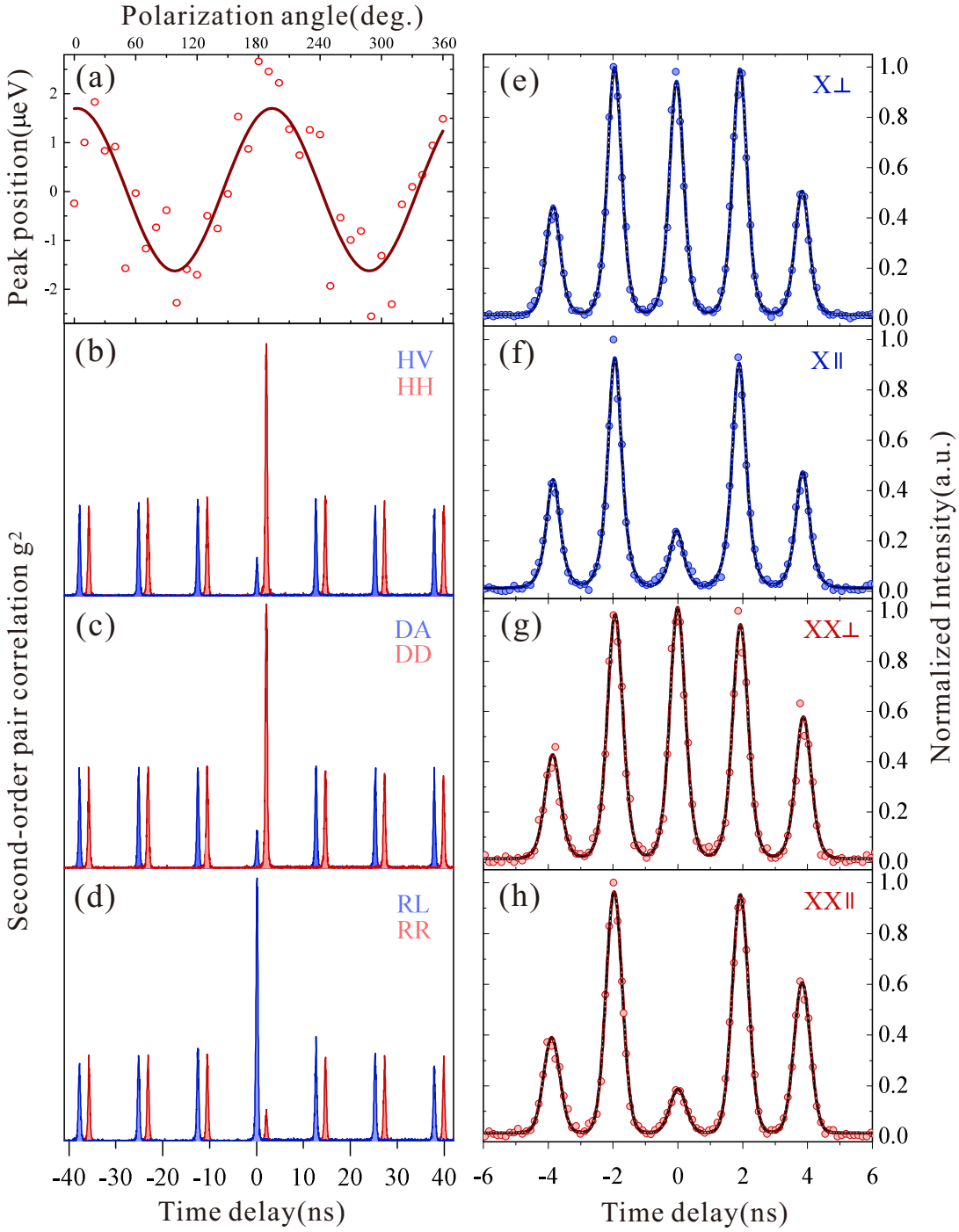


FIG. S9: **Entanglement and indistinguishablity of device 4.** (a) Polarization-dependent measurement to determine the FSS of X. (b), (c) and (d) are the X-XX polarization dependent cross-correlation histogram under "π pulse" conditions for linear, diagonal, and circular basis respectively. Data for cross-polarization configurations are shifted deliberately for clarity. Two-photon interference for cross-polarized (e), co-polarized (f) X photons and cross-polarized (g), co-polarized (h) XX photons.

## XII. DETAILS OF ESTIMATING THE PAIR RATE AND ENTANGLEMENT FIDELITY FOR THE WORK IN TABLE I

In order to make a comparison of the performance between different types of polarization entangled photon pair source, it is necessary to specify how the source characteristics are measured.

For the QD based sources, the pair efficiency is given as the average number of photon pairs per excitation pulse collected into the first lens/objective with a specific numerical aperture, whereas for the SPDC sources it is the same figure of merit but collected into the first fiber. In quantum dot sources, the pair rate is typically calculated from the excitation pulse rate, the setup efficiency and the count rates on the detectors. For parametric down-conversion sources the internal pair generation efficiency is excitation power dependent. Higher excitation power also leads to multi-pair generation, reducing the source fidelity because of the probabilistic nature of the generation. The details of each of the cited work in table I is given below:

*InAs QD in micropillar molecule (Ref. 38)*: the single-photon collection efficiency at the first lens is 0.35 by calculating with the APD count rate and the setup efficiency, therefore a pair rate of 0.35*0.35=0.12 is obtained. The entanglement fidelity of 0.67 is extracted from quantum tomography measurement. This number is very consistent with the fidelity of 0.65 extracted from cross-correlations of X and XX photons at three different polarization basis.

*InAsP QDs in nanowires (Ref. 39)*: the calculated photon pair count rate is 0.2 MHz under a 80 MHz pulsed excitation, which give rises to a pair rate of 0.2/80=0.0025. Because two-photon state is modified by the birefringence induced by the nanowire shape anisotropy, a maximal entangled state $|JJ\rangle + |WW\rangle$ instead of $|HH\rangle + |VV\rangle$ with a fidelity of 0.817 is extracted from quantum state tomography.

*InAs QDs in planar cavities (Ref. 18)*: the calculated single-photon count rate at the first lens is 200-300 kHz under a 75 MHz pulsed excitation, which gives rise to a single-photon collection efficiency of 0.004. Therefore the pair rate is 0.004*0.004$<$0.001. The entanglement fidelity is extracted from cross-correlations of X and XX photons at three different polarization basis.

*GaAs QDs in planar cavities (Ref. 23)*: the calculated single-photon count rate at the first lens is 42 kHz under a 80 MHz pulsed excitation, which gives rise to a single-photon collection efficiency of 0.0005. Therefore the pair rate is 0.0005*0.0005$<$0.001. The entanglement fidelity of 0.94 is extracted from cross-correlations of X and XX photons at three different polarization basis.

*SPDC USTC (Ref. 11)*: a pair count rate of 12 MHz*0.7=8.4 MHz is extracted at the first fiber under a 78 MHz pulsed excitation, which gives rise to a pair rate of 0.105. The entanglement fidelity is extracted from cross-correlations at three different polarization basis.

*SPDC Vienna (Ref. 3)*: pumping the periodically poled potassium titanyl phosphate (ppKTP) crystal by a pulsed laser with a repetition rate of 1 MHz, 3500 pairs are created in the crystal. Considering the coupling loss in the optical fiber, the upper bound on the pair efficiency is $0.0035 < 0.01$. The entanglement fidelity is extracted from cross-correlations at three different polarization basis.

*SPDC Geneva (Ref. 10)*: a pair rate of 0.1 is directly given in the paper. The fidelity to a maximally entangled state was measured in the time-bin basis.

---

* These authors contributed equally
† Correspondence to Armando.Rastelli@jku.at, lijt3@mail.sysu.edu.cn, wangxueh@mail.sysu.edu.cn

[S1] Y. H. Huo, A. Rastelli and O . G. Schmidt, "Ultra-small excitonic fine structure splitting in highly symmetric quantum dots on GaAs (001) substrate," *Appl. Phys. Lett.* **102**,152105 (2013).

[S2] M. Davanco, M. T. Rakher, D. Schuh, A. Badolato and K. Srinivasan, "A circular dielectric grating for vertical extraction of single quantum dot emission," *Appl. Phys. Lett.* **99**, 041102 (2011).

[S3] L. Sapienza, M. Davano, A. Badolato and K. Srinivasan, "Nanoscale optical positioning of single quantum dots for bright and pure single-photon emission," *Nat. Commun.* **6**, 7833 (2015).

[S4] A. J. Hudson, R. M. Stevenson, A. J. Bennett, R. J. Young, C. A. Nicoll, P. Atkinson, K. Cooper, D. A. Ritchie, and A. J. Shields, "Coherence of an Entangled Exciton-Photon State," *Phys. Rev. Lett.* **99**, 266802 (2007).

[S5] B. Urbaszek et al., "Nuclear spin physics in quantum dots: An optical investigation," *Rev. Mod. Phys.* **85**, 79 (2013).

[S6] E. A. Chekhovich et al., "Isotope sensitive measurement of the hole-nuclear spin interaction in quantum dots," *Nature Phys.* **9**, 1 (2011).

[S7] E. A. Chekhovich et al., "Nuclear spin effects in semiconductor quantum dots," *Nature Mater.* **12**, 694 (2013).

[S8] R. Stockill et al., "Quantum dot spin coherence governed by a strained nuclear environment," *Nature Commun.* **7**, 12745 (2016).

[S9] D. Huber et al., "Strain-tunable GaAs quantum dot: An on-demand source of nearly-maximally entangled photon pairs," *Phys. Rev. Lett.* 121, 033902 (2018).

[S10] J. Iles-Smith, D. P. S. McCutcheon, A. Nazir, and J. Mork, "Phonon scattering inhibits simultaneous near-unity efficiency and indistinguishability in semiconductor single-photon sources," *Nature Photon.* **11**, 521 (2017).

[S11] A. Reigue et al., "Probing Electron-Phonon Interaction through Two-Photon Interference in Resonantly Driven Semiconductor Quantum Dots," *Phys. Rev. Lett.* 121, 033902 (2018).

[S12] A. Nazir and D. PS. McCutcheon, "Modelling excitonphonon interactions in optically driven quantum dots," *Journal of Physics: Condensed Matter* 28, 103002 (2016).

[S13] M. Cardona and N. E. Christensen, "Acoustic deformation potentials and heterostructure band offsets in semiconductors," *Phys. Rev. B* 36, 2906 (1987).
[S14] J. S. Blakemore "Semiconducting and other major properties of gallium arsenide," *J. Appl. Phys.* 53, R123 (1982).
[S15] D. PS. McCutcheon and A. Nazir, "Quantum dot Rabi rotations beyond the weak excitonphonon coupling regime," *New J. Phys* 12, 113042 (2016).
[S16] C. Roy and S. Hughes, " Phonon-Dressed Mollow Triplet in the Regime of Cavity Quantum Electrodynamics: Excitation-Induced Dephasing and Nonperturbative Cavity Feeding Effects," *Phys. Rev. Lett.* 106, 247403 (2011).